JPET Fast Forward. Published on October 31, 2018 as DOI: 10.1124/jpet.118.252080
This article has not been copyedited and formatted. The final version may differ from this version.

JPET#252080

# Inhibition of Advanced Glycation End Products Formation Attenuates Cardiac Electrical and Mechanical Remodeling and Vulnerability to Tachyarrhythmias in Diabetic Rats[S]

**Gwo-Jyh Chang, Yung-Hsin Yeh, Wei-Jan Chen, Yu-Shien Ko, Jong-Hwei S. Pang, and Hsiao-Yu Lee**

*Graduate Institute of Clinical Medicinal Sciences, College of Medicine, Chang Gung University, Tao-Yuan, Taiwan (G.J.C., J.H.S.P, H.Y.L), and Cardiovascular Medicine, Chang Gung Memorial Hospital, Tao-Yuan, Taiwan (G.J.C., Y.H.Y., W.J.C, Y.S.K.)*



[S] **This article has supplemental material**

JPET#252080

**Running title:** Inhibition of AGEs attenuates cardiac electrical remodeling

**Corresponding author:** Gwo-Jyh Chang, Graduate Institute of Clinical Medicinal Sciences, College of Medicine, Chang Gung University, 259 Wen-Hwa 1st Road, Kwei-Shan, Tao-Yuan, Taiwan

TEL: 886-3-211-8800 ext. 3481

FAX: 886-3-328-0170

E mail: gjchang@mail.cgu.edu.tw

Number of text pages (includes figure legends, tables, and figures): 44

Number of tables: 2

Number of figures: 9

Number of references: 43

Word number of Abstract: 249

Word number of Introduction: 543

Word number of Discussion: 1498

**Abbreviations**

AERP, atrial effective refractory period; AG, aminoguanidine; AGE, advanced glycation end product; AH, atrio-His bundle conduction interval; APA, action potential amplitude; $APD_{25,\ 50,\ 90}$, action potential duration measured at 25, 50 and 90% repolarization; AVNERP, AV nodal effective refractory period; BCL, basic cycle length; $dP/dt_{max}$ and $dP/dt_{min}$, maximal rate of rise and fall of LV pressure; HPFRP, His-Purkinje system functional refractory period; HV, His-ventricular conduction interval; IACT, interatrial conduction time; $I_{Ca,L}$, L-type $Ca^{2+}$ current; $I_{K1}$, inward rectifier $K^+$ current; $I_{SS}$, steady-state outward $K^+$ current; $I_{to}$, transient outward $K^+$ current; LV, left ventricle; LVDP,LV developed pressure; LVEDP, LV end-diastolic pressure; LVESP, LV end-systolic pressure; NCX, $Na^+$-$Ca^{2+}$ exchanger; PLB, phospholamban; RAGE, AGE receptor; RMP, resting membrane

JPET Fast Forward. Published on October 31, 2018 as DOI: 10.1124/jpet.118.252080
This article has not been copyedited and formatted. The final version may differ from this version.



potential; RyR2, ryanodine receptor $Ca^{2+}$ release channel, SA, stimulus-atrial conduction interval; SERCA, sarco(endo)plasmic reticulum $Ca^{2+}$-ATPase; STZ, streptozotocin; VERP, ventricular effective refractory period; $V_{max}$, maximal upstroke velocity of action potential; WCL, Wenckebach cycle length.

**Recommended section:** Cardiovascular

## Abstract

Diabetic patients with cardiomyopathy show a higher incidence of arrhythmias and sudden death. Chronic hyperglycemia induces the formation of advanced glycation end products (AGEs), which contribute to the pathogenesis of diabetic cardiomyopathy. This study investigated whether inhibition of AGEs formation by aminoguanidine (AG) could prevent the cardiac electromechanical and arrhythmogenic remodeling in diabetes mellitus. Streptozotocin-induced diabetic rats received AG (100 mg/kg daily, IP) or vehicle (normal saline, IP) for 5 weeks. Rats underwent hemodynamic recording to evaluate cardiac function, and heart preparations were used to determine the electrical, mechanical and biochemical functions. *In vitro* high glucose-induced AGEs formation, reactive oxygen species (ROS) generation, and action potential changes were examined in HL-1 atrial cells. AG treatment improved the diabetes-induced depression in left ventricular pressure and the relaxation rate and normalized the prolongation of QTc intervals in anesthetized rats. AG reduced the vulnerabilities to atrial and ventricular tachyarrhythmias in perfused diabetic hearts. AG normalized the prolonged action potential duration in diabetic atrial and ventricular muscles which was correlated with the restoration of both transient outward ($I_{to}$) and steady-state outward ($I_{SS}$) $K^+$ current densities in cardiomyocytes. The abnormal kinetics of $Ca^{2+}$ transients and contraction were reversed in cardiomyocytes from AG-treated diabetic rats, along with parallel preservation of sarco(endo)plasmic reticulum $Ca^{2+}$-ATPase (SERCA2a) expression. Furthermore, e*x vivo* and *in vitro* studies showed AG attenuated AGEs and ROS formation. Thus, long-term administration of AG ameliorated cardiac electromechanical remodeling and arrhythmogenicity in diabetic rats and may present an effective strategy for the prevention of diabetes-associated arrhythmias.

## Introduction

Diabetes mellitus (DM) is associated with an increased risk of cardiovascular morbidity and mortality, much of which stems from cardiomyopathy, a unique disease that can progress towards overt heart failure independent of vascular complications (Bugger and Abel, 2014). Diabetic cardiomyopathy, which can occur in both type 1 and type 2 diabetes even with good glycemic control, is characterized by early-onset diastolic and late-onset systolic dysfunction, as well as ECG abnormalities such as QT prolongation and dispersion (Veglio et al., 2004; Huynh et al., 2014). Such ECG changes may increase the incidence of life-threatening ventricular arrhythmias and sudden death (Veglio et al., 2004). Diabetes is also associated with an increased incidence of atrial fibrillation (Movahed et al., 2005). There is emerging evidence to suggest that defects in intracellular $Ca^{2+}$ homeostasis can contribute to myocardial mechanical and electrical dysfunction (Bugger and Abel, 2014). As a consequence, agents that restore the normal electrical and $Ca^{2+}$ handling properties may represent a useful approach for the prevention of these lethal complications.

Diabetes triggers a number of signaling pathways that lead to the development of cardiomyopathy (Bugger and Abel, 2014). Chronic hyperglycemia is associated with the formation of AGEs, which are biochemical end products of non-enzymatic glycosylation that contribute to diabetic complications (Norton et al., 1996; Brownlee, 2001). Growing evidences suggest that targeting AGEs accumulation may constitute a potential strategy for prevention of cardiomyopathy (Yamagishi et al., 2008; Bodiga et al., 2014). AGEs cause damage to cells, possibly by means of protein modification or interactions with AGE receptors (RAGEs), generating reactive oxygen species (Brownlee, 2001; Bodiga et al., 2014). Oxidative stress plays a crucial role in the pathogenesis of diabetic complications (Huynh et al., 2014), and is a known major modulator of cardiac $K^+$ channels. Under diabetic conditions, the transient outward $K^+$ current ($I_{to}$) density in cardiac cells is down-regulated by oxidative stress (Li et al., 2005) and is augmented following relief of this stress. Modulation of redox signaling is thus an attractive strategy for preventing diabetic cardiac remodeling

(Huynh et al., 2014).

Aminoguanidine (AG), a nucleophilic hydrazine compound, is the prototype and most extensively studied inhibitor of AGEs formation (Brownlee et al., 1986). AG inhibits AGEs formation via trapping of reactive carbonyl intermediates and hence preventing modification of nucleophilic residues in proteins. AG also acts as an inhibitor of inducible NO synthase (Corbett et al., 1992) and as an antioxidant (Giardino et al., 1998). AG-mediated inhibition of the cross-linking of AGEs on collagen molecules has been shown to retard diabetes-associated myocardial stiffness and the decrease in myocardial compliance (Norton et al., 1996). AG therapy has been reported to prevent diabetic cardiac hypertrophy by blocking protein carbonylation (Stadler et al., 2005), and to attenuate contractile dysfunction either by inhibiting the accumulation of AGEs in the arterial wall (Wu et al., 2008) or by decreasing AGEs-induced microtubule stabilization in the myocardium (Yuan et al., 2015). Although these results suggest a potential role for the AGEs inhibitor for prevention of diabetic cardiovascular complications, the effect of this intervention on diabetes-induced cardiac electromechanical and arrhythmogenic remodeling remains unknown. In this study, we comprehensively investigated the effects of long-term AG treatment on the status of cardiac mechanical function and associated $Ca^{2+}$ handling, as well as electrophysiological and arrhythmogenic properties in STZ-induced diabetic rats.



## Materials and Methods

### Animal preparation.

All experiments were approved by the Institutional Animal Care and Use Committee of Chang Gung University and were performed in accordance with the Guide for the Care and Use of Laboratory Animals published by the US National Institutes of Health (NIH publication No 85-23, 8th edition, revised 1996). Male Sprague–Dawley rats (BioLASCO Co., Taipei, Taiwan) weighing 190–220 g, age 6 weeks, received a single tail vein injection of STZ (65 mg/kg). STZ was freshly dissolved in 0.9% saline

containing 0.1 M sodium citrate, pH adjusted to 4.5. One week after STZ injection, animals that had at least a 3-fold increase in fasting plasma blood glucose levels compared to pre-injection levels were classified as diabetic. Blood glucose level was determined by using a digital glucometer and test strips (Ascensia ELITE®, Bayer HealthCare AG, Leverkusen, Germany). Rats injected with comparable volumes of citrate-buffered saline served as nondiabetic controls. Diabetic and control rats were received either AG (100 mg/kg daily, IP) or vehicle (saline, IP), respectively, for 5 weeks in an identical fashion. Rats were housed in a 12-h light/dark cycle animal room and were allowed free access to standard chow and water.

**Hemodynamic and electrocardiogram measurements.**

After the 6-week experimental period, the rats were anesthetized with urethane (1.25 g/kg, IP). Blood pressure was measured by inserting a polyethylene cannula into the femoral artery and connecting it to a pressure transducer with a bridge amplifier. Lead II ECGs were recorded by a biological amplifier. A 1.9F microtip catheter (Scisense, ON, Canada) connected to a pressure–volume conductance system (896B, Scisense) was used to measure left ventricular (LV) pressure. Output signals from these amplifiers were connected to an ACQ16 acquisition system (DSI Ponemah, OH, USA), and were computed using an analysis program (P3 Plus 4.80-SP4; DSI Ponemah).

**Histological analysis.**

The atrial and ventricular sections (5 μm thickness) were stained with Masson's trichrome and viewed under a light microscope (200× amplification; Axio Observer Z1, Carl Zeiss, Germany). The fraction of interstitial fibrosis area was quantified on 5 fields per slice for each heart using Image-Pro Premier 9.0 (Media Cybernetics, MD, USA).

**Electrophysiological studies in perfused hearts.**

Rats were sacrificed after the completion of hemodynamic recordings. The heart was quickly excised, mounted on a Langendorff perfusion apparatus, and retrogradely perfused at a rate of 6 ml/min/(g cardiac tissue) with oxygenated (95% $O_2$ and 5% $CO_2$) normal Tyrode's solution

[composition (mM): 137 NaCl, 5.4 KCl, 1.1 $MgCl_2$, 11.9 $NaHCO_3$, 0.33 $NaH_2PO_4$, 1.8 $CaCl_2$ and 11 dextrose] at 37°C as described previously (Chang et al., 2014). A 1.2F octapolar EP catheter (Scisense) was used to record the His bundle electrogram, and the other platinum electrode was used to record epicardial ventricular signals. To pace the atrium and ventricle, one pacing electrode was placed on the right atrium and the 2$^{nd}$ was placed on the right ventricular apex. Pacing stimuli (1-ms duration, twice-threshold voltage) were delivered by a programmable stimulator (DTU 215; Fischer Imaging, Denver, CO, USA). The signals were continuously recorded on a chart recorder (WindowGraf, Gould Inc., Cleveland, OH, USA), and digitized simultaneously with a data acquisition system (IWX/214, iWorx, Dover, NH, USA). The right atrium was then paced at a constant rate which was slightly faster than the spontaneous heart rate. At this constant rate pacing, the intra-atrial (SA), AV nodal (AH) and His–ventricular (HV) conduction intervals, and QT interval were measured. Incremental right atrial pacing was used to determine the Wenckebach cycle length (WCL), at which the 1:1 AV conduction was lost. Atrial premature extra-stimulation ($S_2$) after a train of constant rate atrial pacing ($S_1S_1$) for 8 beats was then performed to obtain the refractory periods of the atria, AV node, and His–Purkinje system. The ventricular effective refractory period (VERP) was determined using a ventricular extra-stimulation study protocol.

Atrial tachyarrhythmia was induced with 1-s burst pacing (a train of 100 square wave pulses, 1 ms in duration at a frequency of 100 Hz) after 8 regularly paced stimuli ($S_1$) at 200-ms pacing cycle length and 5× diastolic threshold. Ventricular tachyarrhythmia was evoked by programmed electrical extra-stimulation. An arrhythmia scoring system was used as described (details in Supplemental material).

**Electrical measurements on cardiac muscles.**

The left atrial strips or LV papillary muscles were superfused at a rate of 20 ml/min with oxygenated normal Tyrode's solution, and were stimulated with 1.5× threshold strength pulses (pulse duration: 1 ms) through platinum field electrodes (Chang et al., 2014). Transmembrane potentials were recorded using an Axoclamp 2B amplifier (Molecular Devices, CA, USA).

**Measurements of $Ca^{2+}$ transient and cell shortening.**

Single cardiomyocytes were isolated using a modification of the enzymatic dissociation procedure previously described (Chang et al., 2014) (details in Supplementary Materials and Methods). Intracellular $Ca^{2+}$ transients were measured by fura-2 fluorescence at room temperature (25–27°C) as described previously (Chang et al., 2014). Cytosolic loading of fura-2 was achieved by incubating cardiomyocytes with 5 μM fura-2-AM and 2% Pluronic F-127 for 30 min at room temperature. After washing out the excess fura-2-AM, the loaded myocytes were transferred to 1.8 mM $Ca^{2+}$ containing buffer and were stimulated by 2-ms square wave pulses with a voltage approximately 30%–40% above the threshold, at a frequency of 1 Hz. The cells were illuminated at a wavelength of 340 or 380 nm using a RatioMaster fluorometer system (PTI-HORIBA Scientific, NJ, USA). The ratio of the fluorescence signal ($F_{340}/F_{380}$) was used as the indicator of intracellular $Ca^{2+}$ concentration. Cell shortening was measured simultaneously with a video edge-detection system (Crescent Electronics, Sandy, UT, USA). Caffeine-induced $Ca^{2+}$ transients were evoked by rapidly bath application of 10 mM caffeine 10 s after stopping field stimulations of the myocytes with electrical pulses (for 20 s at 1-Hz frequency) to ensure stable SR $Ca^{2+}$ load.

**Western blot analysis.**

Western blotting was performed to measure the expression of various proteins in LV samples or HL-1 cells using primary antibodies against ryanodine receptor $Ca^{2+}$ release channel (RyR2) (Thermo Fisher Scientific, MA, USA), SERCA2a (Badrilla, Leeds, UK), phospholamban (PLB) (Badrilla), phosphorylated $pSer^{16}$-PLB (Millipore, CA, USA), $Na^{+}/Ca^{2+}$ exchanger (NCX1) (Santa Cruz Biotech, CA, USA), AGE (TransGenic, Fukuoka, Japan), or RAGE (Abcam, MA, USA). The blot probed with GAPDH (Santa Cruz) or tubulin antibody (Santa Cruz) was used as an internal control. Details are described in Supplemental material.

**Detection of NADPH-dependent superoxide production by chemiluminescence.**

Generation of superoxide was estimated in fresh LV tissue (approximately 2 mg) with

lucigenin-enhanced chemiluminescence using a luminometer (Plate CHAMELEON, Hidex, Finland) as previously described (Yeh et al., 2016). Photon outputs were measured after addition of lucigenin (5 μM) and NADPH (100 μM). Chemiluminescence data were recorded from 5 tissues for each heart and normalized to the dry weight of tissues.

***In vitro* transfection of small interfering (si) RNA.**

HL-1 atrial myocytes in 4-well dishes were transfected with chemically synthesized siRNAs for RAGE, or its control siRNA (200 nM/well; Dharmacon Lafayette, CO, USA) for 48 h prior to cell treatment using DharmaFECT 1 (Dharmacon) according to the manufacturer's instructions (Yeh et al., 2016). The on-target siRNA-smart pool included four sequences.

**Detection of intracellular reactive oxygen species (ROS).**

Intracellular ROS generation in HL-1 cells was measured using cell-permeable fluorescent dyes [2, 7-dichlorodihydrofluorescein diacetate (DCF-DA) or dihydroethidium (DHE)] at a concentration of 10 μM (Yeh et al., 2016). The ROS-mediated fluorescence was observed under a confocal microscope (Leica TCS SP2, Wetzlar, Germany) with excitation using a 488-nm argon laser. Emission was recorded using a long-pass > 530-nm filter set to acquire two-dimensional images (512 × 512 pixels).

**Whole-cell patch-clamp recording.**

Ionic currents were recorded in LV or atrial myocytes at room temperature (25–27°C) using the whole-cell patch-clamp configuration (pipette resistance of 2–5 MΩ) as previously described (Chang et al., 2014). Action potentials of single HL-1 cells were recorded in the current-clamp mode at a rate of 1 Hz. Membrane currents and potentials were recorded using an integrating patch clamp amplifier (Axopatch 200B, Molecular Devices). Command pulses were generated by a 16-bit Digidata 1320A D/A converter (Molecular Devices) controlled by pCLAMP8.0.2 software (Molecular Devices). Data acquisition and analysis were performed using the Clampex and Clampfit module of pCLAMP software, respectively. Recordings were filtered at 10 kHz and acquired at 100 kHz. After forming

the whole-cell recording configuration, a capacitive transient induced by a 10 mV step from a holding voltage of 0 mV was recorded and used for the calculation of cell capacitance. Series resistance was in the range of 4–6 MΩ and was compensated by 60% to 80%. Solution contents and pulse protocols for recording of specific ionic current are described in Supplemental material.

**Chemicals.**

All chemicals used were purchased from Sigma-Aldrich (St Louis, MO, USA) except for fura-2/AM and Pluronic F127 were purchased from Molecular Probes (Eugene, OR, USA). Fura-2/AM and Pluronic F127 were dissolved in dimethylsulfoxide (DMSO). Other drugs were dissolved in physiological saline before the start of the experiment.

**Statistical analysis.**

Data are expressed as the means ± SEM. Statistical analysis was carried out by one-way ANOVA followed by post-hoc Tukey's test for multiple comparisons. $P < 0.05$ was considered statistically significant. Sigmaplot 12.0 (Systat Software, Inc., Chicago, IL, USA) was used for fitting data with Boltzmann or other user-defined functions.

## Results

**General features of experimental animals.**

During the sixth week after STZ injection, vehicle-treated diabetic rats had markedly lower body weight and higher fasting blood glucose levels compared with the age-matched nondiabetic controls. There was no significant change in body weight gain or blood glucose levels in either the diabetic or control group after AG administration for 5 weeks (Table 1). Diabetes was associated with lower LV weight (LVW) and heart weight (HW) that were attributable to lower body weight (BW). AG-treated diabetic rats showed a significant decrease in LVW and HW, but did not differ significantly in BW from the untreated diabetic group. The atrial weight (AW)/BW, LVW/BW, and HW/BW ratios in the diabetic rats were significantly higher compared with those of nondiabetic

controls, and were reduced by treatment with AG (Table 1).

Representative left atrial and ventricular tissue sections from each group stained with Masson's trichrome are shown in Supplemental Fig. S1A. The amount of fibrosis in both tissues, as a percentage of perimuscular interstitial blue area (except muscle for each rat heart), was significantly higher in the vehicle-treated diabetic group than in the control group (Supplemental Fig. S1, B and C). There was a significant reduction in cardiac fibrosis in AG-treated rats compared with their vehicle-treated diabetic counterparts.

**Effects of AG on hemodynamic and electrocardiographic indices.**

Diabetic rats had significantly decreased heart rate, LV end-systolic (LVESP) and developed pressure (LVDP), and maximal rate of rise ($dP/dt_{max}$) and fall ($dP/dt_{min}$) of LV pressure compared to nondiabetic controls. Diabetic rats also showed increased end-diastolic pressure (LVEDP) and relaxation time constant (Tau) of LV. AG-treated diabetic rats exhibited improved LVESP, LVDP, and relaxation Tau (Fig. 1A; Table 1), and also showed a trend towards higher LV $dP/dt_{max}$ and $dP/dt_{min}$, and lower LVEDP, but heart rates were not affected. AG administration significantly attenuated the prolongation of the QTc interval ($P < 0.001$) in diabetic rats (Fig. 1A, Table 1). Other parameters were similar in all groups. AG treatment had no significant effect on any measured parameters in nondiabetic controls.

**Effects of AG on the intracardiac conduction system.**

Langendorff-perfused diabetic hearts had longer basic cycle length (BCL), QT intervals and refractory periods of the atrium (AERP), AV node (AVNERP), His–Purkinje system (HPFRP) and ventricle (VERP) compared with nondiabetic controls (Fig. 1B; Table 2). No changes in other parameters were observed in any group. Administration of AG significantly prevented the prolongation of the QT interval, AERP, HPFRP, and VERP in diabetic hearts. However, AG-treated diabetic rats showed a nonsignificant trend towards shorter BCL and AVNERP.

**Effects of AG on susceptibility to atrial and ventricular tachyarrhythmias.**

Only a small number of atrial tachyarrhythmias (AT) were induced in control hearts. In contrast, the same stimulation induced a much longer duration of AT in diabetic hearts, along with a wide range in the values of this parameter (Fig. 2, A and B). The interatrial conduction time (IACT) was significantly longer in diabetic hearts than in controls (Fig. 2C). AG administration significantly reduced the duration of AT with normalization to IACT in diabetic hearts but did not affect the AT vulnerability and IACT in the control group.

Representative recordings of the induction of ventricular tachyarrhythmias are shown in Fig. 2D. Control rats with or without AG treatment had very low arrhythmia scores (Fig. 2, D and E). In contrast, the inducibility quotient was significantly higher in diabetic hearts vs. controls and was decreased by AG treatment.

**Effects of AG on action potential characteristics in ventricular and atrial tissues.**

Representative recordings of ventricular action potentials during stimulation at 1 and 4 Hz are shown in Fig. 3A. The diabetic group had significantly prolonged action potential durations at the 25%, 50% and 90% repolarization levels ($APD_{25}$, $APD_{50}$, and $APD_{90}$) at all pacing frequencies tested (0.5 to 4 Hz) compared with those of the control group (Fig. 3, A and B). The maximal depolarization velocity ($V_{max}$) was lower in diabetic muscles compared to that of controls at each frequency (Fig. 3B). Administration of AG attenuated the prolongation of APD and decreased $V_{max}$ in diabetic rats, but had no effect in the control group. Other parameters were not affected by either diabetes or AG treatment. Similar but smaller changes in APD and $V_{max}$ were also observed in atrial strips from diabetic rats (Supplemental Fig. S2). AG attenuated the prolongation of $APD_{50}$ and $APD_{90}$ and depression of $V_{max}$, and also tended to attenuate the prolongation of $APD_{25}$ in the diabetic group.

**Effects of AG on cell shortening and relengthening, and $Ca^{2+}$ transients in cardiomyocytes.**

Diastolic cell lengths were smaller in LV myocytes from the diabetic group treated with vehicle or AG. Diabetic myocytes had significantly prolonged time-to-peak shortening and

JPET Fast Forward. Published on October 31, 2018 as DOI: 10.1124/jpet.118.252080
This article has not been copyedited and formatted. The final version may differ from this version.



time-to-50% relengthening, and showed a trend towards smaller fractional shortening compared with those of controls (Fig. 4, A and C). Fura-2 fluorescence data showed that diabetic myocytes displayed higher diastolic $Ca^{2+}$ transient levels associated with longer times to peak and decay times of the $Ca^{2+}$ transient than did controls (Fig. 4, A and B). In parallel with the fractional shortening, diabetic myocytes also showed a trend towards lower $Ca^{2+}$ transient amplitude. AG administration significantly reversed the abnormal kinetic parameters of cell shortening/relengthening and $Ca^{2+}$ transients in diabetic myocytes. None of these parameters changed in the AG-treated control myocytes. Similar results on the basic properties of $Ca^{2+}$ transients and cell contraction were observed in atrial myocytes from various groups (Supplemental Fig. S3). However, the amplitude of $Ca^{2+}$ transients was significantly lower in the diabetic group compared to the controls.

To assess the sarcoplasmic reticulum (SR) $Ca^{2+}$ content, we rapidly applied caffeine (10 mM) 10 s after cessation of electrical stimulation (Fig. 5). LV myocytes from diabetic rats had a tendency towards a smaller caffeine-induced $Ca^{2+}$ transient amplitude, together with a markedly longer decay time constant compared with those of the controls. AG treatment partially attenuated the prolonged decay time in diabetic myocytes.

**Effects of AG on the expression of $Ca^{2+}$ handling proteins.**

There was a significant decrease in the expression of SERCA2a protein in LV tissues from diabetic rats compared to the nondiabetic control group, whereas PLB (total and phosphorylated), RyR2, and NCX were unchanged (Fig. 6, A–E). AG administration significantly restored the expression of SERCA2a but did not affect the levels of PLB, $pSer^{16}$-PLB, RyR2, and NCX in diabetic tissues. AG treatment did not affect the expression of any protein tested in the control group.

**Effects of AG on AGEs accumulation and superoxide production in LV tissues.**

There was a significant increase in the level of AGEs in LV tissues of diabetic rats, and this was attenuated after AG treatment (Fig. 6F). AG had no effect on AGE levels in control rats. The

NADPH-dependent superoxide production in LV tissues (10 rats per group) was evaluated using a lucigenin-enhanced chemiluminescence technique and expressed as values relative to control group. Diabetes induced a 1.75 ± 0.09-fold increase in superoxide generation compared to controls ($P < 0.001$). AG treatment attenuated diabetes-induced superoxide production (1.29 ± 0.14 fold, $P < 0.05$ vs DM+Veh group), but it did not affect the level in control rats (1.02 ± 0.09 fold).

**Effects of AG on high glucose (HG)-induced AGEs formation, oxidative stress, and APD prolongation in HL-1 atrial cells.**

To further explore the effect of AG on diabetes-induced AGEs and ROS production *in vitro*, we treated HL-1 cells with HG (25 mM) to model the diabetic condition. Mannitol (19.4 mM) with normal glucose (NG, 5.6 mM) was used in parallel to test whether the effect of high glucose was simply due to changes in medium osmolality. Western blotting and fluorescence study showed that HG incubation enhanced the AGEs and ROS production, and this increase was significantly attenuated by AG (1 μM) treatment (Fig. 7, A and B). The increase of AGEs and ROS production was not related to increased osmolality since mannitol did not affect this effect. In order to explore the role of RAGE in AGEs-mediated effects, cells were transfected with siRNA-RAGE for 48 h to silence RAGE, and then incubated with HG for 24 h. Knockdown of RAGE was confirmed by a decrease in RAGE protein level. AG administration had no effect on RAGE expression either in control or RAGE gene knockdown cells (Fig. 7C). Knockdown of the RAGE gene significantly attenuated HG-induced production of ROS (Fig. 7D). AG treatment in control cells induced a slightly higher decrease in HG-induced ROS production compared to cells with RAGE gene knockdown. Moreover, AG administration further decreased ROS production in RAGE gene knockdown cells (Fig. 7D), which could be due to the less AGEs to interact with the residual RAGE.

**Effects of AG on high glucose (HG)-induced APD prolongation in HL-1 atrial cells.**

To evaluate the effect of AG on the changes in APD under HG conditions and whether this

effect was related to the AGE-RAGE pathway, the action potentials were recorded in HL-1 cells incubated with NG or HG and in cells cultured in HG with or without RAGE gene knockdown as described above. Electrophysiological features of murine HL-1 cells resemble those of primary cardiomyocytes, with many typical ionic currents including $I_{Na}$, $I_{to}$, $I_{Ca}$, and the rapidly activating $I_K$ ($I_{Kr}$) (Yang et al., 2005). The APD was longer in cells cultured in HG compared in cells cultured in NG (Fig. 8A and B). The prolongation of APD was partially attenuated by AG (1 μM) treatment (Fig. 8, A and B). Incubation with mannitol had no effect on APD. Knockdown of the RAGE gene alone attenuated the prolongation of APD in cells cultured in HG (Fig. 8C and D). AG treatment in control (Con si) cells attenuated HG-induced prolongation of APD. AG administration further tended to attenuate the prolongation of APD in RAGE gene knockdown cells cultured in HG (Fig. 8D).

**Effects of AG on whole-cell $K^+$ currents in cardiomyocytes.**

The current densities of both $I_{to}$ and $I_{SS}$ were considerably smaller in LV myocytes isolated from diabetic hearts compared with those from controls at each voltage. However, the inward rectifier $K^+$ current ($I_{K1}$) density was not significantly changed in the diabetic group (Fig. 9, A–C). AG treatment of the diabetic rats significantly restored densities of both $I_{to}$ and $I_{SS}$. Neither $I_{to}$ nor $I_{SS}$ density was altered following AG administration in the control group. Similar results in *I–V* relationships were observed in atrial myocytes isolated from animals in various groups (Supplemental Fig. S4). The rate of decay of $I_{to}$ at each voltage in LV myocytes was not significantly affected either by diabetes or by AG treatment (Fig. 9D).

The normalized conductance–voltage curves were calculated from the $I_{to}$ amplitude in Fig. 9B. The estimated maximal $I_{to}$ channel conductance ($G_{to,\,max}$) was significantly smaller in diabetic LV myocytes than in controls, and was partially restored by AG treatment (Supplemental Table S1). Neither diabetes nor AG treatment modified the steady-state activation curve, or made a significant difference in the half-activation potential ($V_h$) or slope factor ($k$) between the groups (Fig. 9E,

Supplemental Table S1). The voltage-dependence of steady-state inactivation of $I_{to}$ was measured by a double-pulse protocol (Fig. 9F inset). Similarly, neither diabetes nor AG treatment significantly altered the steady-state inactivation curve, and there was no difference in the half-inactivation $V_h$ or $k$ value between the groups (Fig. 9F; Supplemental Table S1).

To test the possibility that the decrease in $I_{to}$ density is a change in the time-dependence of recovery from inactivation, we studied the recovery properties of $I_{to}$ using a paired-pulse protocol (Fig. 9G inset). The results are shown in Fig. 9G, where the fraction of recovery current amplitude is reported as a function of recovery time. Fitting data with a monoexponential function of these curves enables derivation of similar recovery time constants in all groups (Supplemental Table S1).

**Effects of AG on L-type $Ca^{2+}$ current ($I_{Ca,L}$) in LV myocytes.**

Families of representative $I_{Ca,L}$ current traces from various groups are shown in Supplemental Fig. S5A. The peak current density of $I_{Ca,L}$ at different membrane potentials is quantified in an *I–V* relation plot (Supplemental Fig. S5B). There were no significant differences in *I–V* relation between the control and diabetic groups at all voltages. There was also no significant difference in the time course of the fast and slow components of $I_{Ca,L}$ inactivation. AG administration did not affect the *I–V* curve and inactivation time courses in both the control and diabetic groups. Similarly, there were no differences in the voltage-dependency of the steady-state activation and inactivation or in the recovery from inactivation kinetics (Supplemental Fig. S5, C and D) of $I_{Ca,L}$ among each group. All the mean data are presented in Supplemental Table S1.

## Discussion

The major finding of this study is that treatment with AG, a prototype inhibitor of AGEs formation, markedly protected against the electromechanical remodeling that leads to cardiac dysfunction and arrhythmogenesis in diabetic rats. AG attenuated cardiac hypertrophy and fibrosis, improved both diastolic and systolic function, attenuated abnormal $Ca^{2+}$ handling and cell

contraction kinetics, normalized the changes in the repolarization phase of action potentials, and restored $K^+$ currents in diabetic hearts, by primarily inhibiting AGEs and ROS formation.

Both diastolic and systolic dysfunction have been described in patients and experimental animals with type 1 and type 2 diabetes (Bugger and Abel, 2014; Huynh et al., 2014). The present *in vivo* study demonstrated that diabetes was associated with impaired ventricular relaxation and depressed systolic performance. AG administration offered significant hemodynamic benefits although it only mildly improved LV contractility ($dP/dt_{max}$). We also observed that the most significant changes in contraction and the $Ca^{2+}$ transient in diabetic cardiomyocytes were the increases in rising and decay time, which characterize the most consistent hallmark of diabetic cardiomyopathy (Choi et al., 2002; Yaras et al., 2005; Shao et al., 2007; Zhang et al., 2008). The initial global diastolic dysfunction could be mainly related to impaired relaxation of myocytes, although mild LV fibrosis could also contribute. Intervention with AG could ameliorate these diastolic changes. Since the amplitudes of $Ca^{2+}$ transients, SR $Ca^{2+}$ content, and shortening of diabetic LV myocytes were not significantly impaired as reported previously (Ishikawa et al., 1999; Zhang et al., 2008), the systolic dysfunction may not be simply attributable to defects of the myocytes. It is likely that myocyte apoptosis (Sorrentino et al., 2017), which could be attenuated by AG treatment (Shi et al., 2013), as well as other non-cardiomyocyte factors, may play a predominant role in the present stage of diabetes.

During the excitation–contraction coupling process, SR SERCA2a facilitates relaxation and thereby makes $Ca^{2+}$ available for the next wave of contraction (Bers, 2002). Phosphorylation of SERCA2a inhibitor, PLB, relieves the inhibitory effect exerted by PLB, which enhances $Ca^{2+}$ uptake. The unchanged $I_{Ca,L}$ observed in diabetic myocytes suggests that alterations in $Ca^{2+}$ handling are mediated by altered SR release/uptake mechanisms. The increase in rising time of both the $Ca^{2+}$ transient and contraction in diabetic myocytes may be partly due to the altered function and/or expression of RyR2 on SR (Choi et al., 2002; Yaras et al., 2005). Our data showed no major changes in RyR2 expression in diabetic hearts, suggesting that the defect in RyR2 function, which may caused by its cross-linking with AGEs (Bidasee et al., 2003), may be a contributory factor. Therefore,

AG-mediated restoration of RyR2 function is likely caused via inhibition of AGEs formation. Diabetic heart is characterized by compromised function and expression of SERCA2a (Zhong et al., 2001; Choi et al., 2002; Bidasee et al., 2004). Our current finding of an overt reduction in SERCA2a protein despite unchanged levels of PLB could explain the diabetes-induced delayed $Ca^{2+}$ clearing and relaxation. AG effectively normalized these altered kinetics partially mediated by the restoration of SERCA2a levels or by attenuating AGEs formation and their subsequent cross-linking on SERCA2a (Bidasee et al., 2004) or AGE–RAGE mediated activity (Petrova et al., 2002). We also found that the decay rate of the caffeine-induced $Ca^{2+}$ transient, which reflects the ability of $Ca^{2+}$ extrusion of NCX (Sorrentino et al., 2017), was slower in diabetic myocytes, implying that despite normal expression, NCX activity may be impaired, and this could be partially restored with AG treatment. Overall, AG administration should be expected to prevent the disturbance of $Ca^{2+}$ homeostasis through the restoration of function or expression of $Ca^{2+}$ handling proteins.

The important role of AGE-RAGE axis in diabetic cardiomyopathy has been revealed in RAGE gene-knockdown diabetic mice (Ma et al., 2009). The interaction of AGEs and RAGE may activate a diverse array of signals associated with increased oxidative stress and inflammation, and impaired $Ca^{2+}$ homeostasis (Brownlee, 2001; Bodiga et al., 2014). In cultured HL-1 cells, we demonstrated that HG enhanced formation of AGEs as well as ROS production, which is in line with the findings from *in vivo* diabetes. Increased ROS production could be attenuated by knockdown of the RAGE gene or by AG treatment, suggesting that interaction of AGEs with RAGE could trigger this response. Similar mechanism could explain why the restoration of prolonged APD by AG was mimicked by knockdown of the RAGE gene in HG-cultured cell model. On the other hand, RAGE activation has been shown to enhance NO production and cell damage by upregulation of iNOS (Sumi and Ignarro, 2004; Hegab et al., 2017). However, a previous study showed no increase in NO production in STZ-induced diabetic rat heart (Stadler et al., 2005), implicating that the protective effect of AG in diabetic heart may not necessarily due to iNOS inhibition.

Our results showed a substantial prolongation in APD in diabetic atrial and ventricular

preparations as reported previously (Pacher et al., 1999; Howarth et al., 2009). The longer QTc interval and VERP in diabetic rats was closely correlated with the longer ventricular APD. Lengthening of the APD in diabetes results mainly from a decrease in $I_{to}$ and, to a lesser extent, $I_{SS}$ and/or delayed outward $K^+$ current ($I_K$) (Jourdon and Feuvray, 1993; Wang et al., 1995; Li et al., 2005). Our study confirmed a depression of $I_{to}$ and $I_{SS}$ densities in diabetic myocytes. The decrease in peak $I_{to}$ density could result from either a lower density of $I_{to}$ channels (Qin et al., 2001; Howarth et al., 2009) or from modified properties of single channels—or both. Since we found no significant changes in the kinetics of activation, inactivation, or recovery of $I_{to}$, the former possibility seems to be more likely. The most innovative finding of our study is that AG treatment markedly normalized the prolonged QT interval and APD in diabetic rats, mainly through the restoration of $I_{to}$ and $I_{SS}$ densities possibly by attenuating ROS production. Our cultured cell study further reinforce the notion that the AGE-RAGE-ROS axis may involved in the HG-induced remodeling of APD, although other pathways such as glycosylation of $K^+$ channels should also be considered. We and others (Yaras et al., 2005; Shao et al., 2007) also found no significant differences in densities or any kinetic properties of $I_{Ca,L}$ between the control and diabetic groups, which exclude its putative role in the prolongation of APD. Additionally, AG improved the diminished $V_{max}$ in diabetic cardiac muscles, which could partially explain the restorations of myocardial refractoriness and interatrial conduction function.

Previous studies showed that delayed atrial conduction and increased fibrotic deposition in the atria play a major role in promoting atrial tachyarrhythmias in diabetic rats (Kato et al., 2006). Recently, Watanabe et al. (2012) suggested that the increased spatial dispersion and alternans of atrial APD may also be key mechanisms. Our study showed that the interatrial conduction time and AERP were significantly longer, and were combined with interstitial fibrosis in diabetic rat hearts. Since moderate AERP prolongation seemed to be a factor against arrhythmogenesis, our results implied that the prominent conduction delay may be a major substrate for atrial tachyarrhythmias. Furthermore, the longer APD in diabetic atrial and ventricular preparations may produce early after-depolarizations

JPET Fast Forward. Published on October 31, 2018 as DOI: 10.1124/jpet.118.252080
This article has not been copyedited and formatted. The final version may differ from this version.



(Lacombe et al., 2007), while the abnormal subcellular $Ca^{2+}$ handling may predispose to delayed after-depolarizations, both of which may further promote arrhythmogenic triggered activities. Thus, we suggest that AG attenuates arrhythmogenic vulnerabilities, presumably via the prevention of abnormal structural remodeling, conduction velocity, AP duration, and $Ca^{2+}$ handling.

Under hyperglycemic settings, the accelerated accumulation of AGEs in tissues plays an important role in the pathogenic process of diabetes and its complications. Moreover, the levels of plasma AGEs reflect the severity of the diabetic complications and independently predict mortality or hospitalization for diabetic patients compromised with heart failure (Willemsen et al., 2012). Thus, intervention with AG aimed at decreasing AGEs should confer clinical relevance and would be a novel approach to prevent the AGEs-mediated electrical and $Ca^{2+}$ handling disorders in diabetic patients. By using a low to moderate dosage of AG (100 mg/kg/day), which was adopted from that used in experimental studies (range: 25-500 mg/kg/day), a beneficial anti-remodeling effect was achieved in our diabetic rat model. Much lower doses (~25-50-fold lower) recommended for use in humans should be expected according to the consideration scale phenomenon (Mordenti et al., 1986). Effective and tolerated dosage levels for AG in management of patients with diabetic cardiomyopathy still need to be determined.

In summary, this study presented the first evidence that chronic administration of AG normalizes the electrical remodeling of the diabetic heart by restoring the diminished $K^+$ current density, and resolves mechanical dysfunctions by restoring the altered kinetics of $Ca^{2+}$ handling and structural remodeling. AG-mediated attenuation of the atrial and ventricular arrhythmogenicities may be primarily attributed to its anti-remodeling effects. There remains a lack of choice of therapies for managing the remodeling specifically in diabetic heart. Our findings provide insights into the novel mechanisms underlying the cardioprotective action of AGEs-formation inhibitors, and have important implications for preventing the diabetes-related cardiac dysfunction and arrhythmias.

## Acknowledgements

The authors thank Ms Shi-Han Weng, Ms Shang-Yu Tsai, Ms Yu-Ting Liu, Ms Chia-Ling Chen, Ms Yu-Ci Liao, Ms Ting-Hsiang Chan, and Ms Wei-Chun Chen for technical assistance.

**Authorship Contributions**

*Participated in research design:* Chang, Yeh.

*Conducted experiments:* Chang, Yeh, Chen, Ko, S. Pang, Lee.

*Performed data analysis:* Chang, Yeh, Lee.

*Wrote or contributed to the writing of the manuscript:* Chang.

## References

Bers DM (2002). Cardiac excitation-contraction coupling. *Nature* **415**:198–205.

Bidasee KR, Nallani K, Yu Y, Cocklin RR, Zhang Y, Wang M, Dincer UD, and Besch HR Jr (2003) Chronic diabetes increases advanced glycation end products on cardiac ryanodine receptors/calcium-release channels. *Diabetes* **52**:1825–1836.

Bidasee KR, Zhang Y, Shao CH, Wang M, Patel KP, Dincer UD, and Besch HR Jr (2004) Diabetes increases formation of advanced glycation end products on sarco(endo)plasmic reticulum $Ca^{2+}$-ATPase. *Diabetes* **53**:463–473.

Bodiga VL, Eda SR, and Bodiga S (2014) Advanced glycation end products: role in pathology of diabetic cardiomyopathy. *Heart Fail Rev* **19**:49–63.

Brownlee M (2001) Biochemistry and molecular cell biology of diabetic complications. *Nature* **414**:813–820.

Brownlee M, Vlassara H, Kooney A, Ulrich P, and Cerami A (1986) Aminoguanidine prevents diabetes-induced arterial wall protein cross-linking. *Science* **232**:1629–1632.

Bugger H and Abel ED (2014) Molecular mechanisms of diabetic cardiomyopathy. *Diabetologia* **57**:660–671.

Chang GJ, Yeh YH, Lin TP, Chang CJ, and Chen WJ (2014) Electromechanical and atrial and ventricular antiarrhythmic actions of CIJ-3-2F, a novel benzyl-furoquinoline vasodilator in rat heart. *Br J Pharmacol* **171**:3918–3937.

Choi KM, Zhong Y, Hoit BD, Grupp IL, Hahn H, and Dilly KW, Guatimosim S, Lederer WJ, Matlib MA (2002) Defective intracellular $Ca^{2+}$ signaling contributes to cardiomyopathy in Type 1 diabetic rats. *Am J Physiol Heart Circ Physiol* **283**:H1398–H1408.

Corbett JA, Tilton RG, Chang K, Hasan KS, Ido Y, Wang JL, Sweetland MA, Lancaster JR,

Williamson JR, and Mcdaniel ML (1992) Aminoguanidine, a novel inhibitor of nitric oxide formation, prevents diabetic vascular dysfunction. *Diabetes* **41**:552–556.

Giardino I, Fard AK, Hatchell DL, and Brownlee M (1998) Aminoguanidine inhibits reactive oxygen species formation, lipid peroxidation, and oxidant-induced apoptosis. *Diabetes* **47**:1114–1120.

Hegab Z, Mohamed TMA, Stafford N, Mamas M, Cartwright EJ, and Oceandy D (2017) Advanced glycation end products reduce the calcium transient in cardiomyocytes by increasing production of reactive oxygen species and nitric oxide. *FEBS Open Bio* **7**:1672–1685.

Howarth FC, Jacobson M, Qureshi MA, Shafiullah M, Hameed RS, Zilahi E, Al Haj A, Nowotny N, and Adeghate E (2009) Altered gene expression may underlie prolonged duration of the QT interval and ventricular action potential in streptozotocin-induced diabetic rat heart. *Mol Cell Biochem* **328**:57–65.

Huynh K, Bernardo BC, McMullen JR, and Ritchie RH (2014) Diabetic cardiomyopathy: mechanisms and new treatment strategies targeting antioxidant signaling pathways. *Pharmacol Ther* **142**:375–415.

Ishikawa T, Kajiwara H, and Kurihara S (1999) Alterations in contractile properties and $Ca^{2+}$ handling in streptozotocin-induced diabetic rat myocardium. *Am J Physiol Heart Circ Physiol* **277**:H2186–H2194.

Jourdon P and Feuvray D (1993) Calcium and potassium currents in ventricular myocytes isolated from diabetic rats. *J Physiol* **470**:411–429.

Kato T, Yamashita T, Sekiguchi A, Sagara K, Takamura M, Takata S, Kaneko S, Aizawa T, and Fu LT (2006) What are arrhythmogenic substrates in diabetic rat atria? *J Cardiovasc Electrophysiol* **17**:890–894.

Lacombe VA, Viatchenko-Karpinski S, Terentyev D, Sridhar A, Emani S, Bonagura JD, Feldman

DS, Györke S, and Carnes CA (2007) Mechanisms of impaired calcium handling underlying subclinical diastolic dysfunction in diabetes. *Am J Physiol Regu Integr Comp Physiol* **293**:R1787–R1797.

Li X, Xu Z, Li S, and Rozanski GJ (2005) Redox regulation of $I_{to}$ remodeling in diabetic heart. *Am J Physiol Heart Circ Physiol* **288**:H1417–H1424.

Ma H, Li SY, Xu P, Babcock SA, Dolence EK, Brownlee M, Li J, and Ren J (2009) Advanced glycation endproduct (AGE) accumulation and AGE receptor (RAGE) up-regulation contribute to the onset of diabetic cardiomyopathy. *J Cell Mol Med* **13**:1751–1764.

Mordenti J (1986) Man versus beast: Pharmacokinetic scaling in mammals. *J Pharma Sci* **75**:1028–1040.

Movahed MR, Hashemzadeh M, and Jamal MM (2005) Diabetes mellitus is a strong, independent risk for atrial fibrillation and flutter in addition to other cardiovascular disease. *Int J Cardiol* **105**:315–318.

Norton GR, Candy G, and Woodiwiss AJ (1996) Aminoguanidine prevents the decreased myocardial compliance produced by streptozotocin-induced diabetes mellitus in rats. *Circulation* **93**:1905–1912.

Pacher P, Ungvári Z, Nánási PP, and Kecskeméti V (1999) Electrophysiological changes in rat ventricular and atrial myocardium at different stages of experimental diabetes. *Acta Physiol Scand* **166**:7–13.

Petrova R, Yamamoto Y, Muraki K, Yonekura H, Sakurai S, Watanabe T, Li H, Takeuchi M, Makita Z, Kato I, Takasawa S, Okamoto H, Imaizumi Y, and Yamamoto H (2002) Advanced glycation endproduct-induced calcium handling impairment in mouse cardiac myocytes. *J Mol Cell Cardiol* **34**:1425–1431.

Qin D, Huang B, Deng L, El-Adawi H, Ganguly K, Sowers JR, and El-Sherif N (2001) Downregulation of $K^+$ channel genes expression in type I diabetic cardiomyopathy. *Biochem Biophys Res Commun* **283**:549–553.

Shao CH, Rozanski GJ, Patel KP, and Bidasee KR (2007) Dyssynchronous (non-uniform) $Ca^{2+}$ release in myocytes from streptozotocin-induced diabetic rats. *J Mol Cell Cardiol* **42**:234–246.

Shi FH, Cheng YS, Dai DZ, Peng HJ, Cong XD, and Dai Y (2013) Depressed calcium-handling proteins due to endoplasmic reticulum stress and apoptosis in the diabetic heart are attenuated by argirein. *Naunyn Schmiedeberg's Arch Pharmacol* **386**:521–531.

Sorrentino A, Borghetti G, Zhou Y, Cannata A, Meo M, Signore S, Anversa P, Leri A, Goichberg P, Qanud K, Jacobson JT, Hintze TH, and Rota M (2017) Hyperglycemia induces defective $Ca^{2+}$ homeostasis in cardiomyocytes. *Am J Physiol Heart Circ Physiol* **312**:H150–H161.

Stadler K, Jenei V, Somogyi A, and Jakus J (2005) Beneficial effects of aminoguanidine on the cardiovascular system of diabetic rats. *Diabetes Metab Res Rev* **21**:189–196.

Sumi D and Ignarro LJ (2004) Regulation of inducible nitric oxide synthase expression in advanced glycation end product-stimulated raw 264.7 cells: the role of heme oxygenase-1 and endogenous nitric oxide. *Diabetes* **53**:1841–1850.

Veglio M, Chinaglia A, and Cavallo-Perin P (2004) QT interval, cardiovascular risk factors and risk of death in diabetes. *J Endocrinol Invest* **27**:175–181.

Wang DW, Kiyosue T, Shigematsu S, and Arita M (1995) Abnormalities of $K^+$ and $Ca^{2+}$ currents in ventricular myocytes from rats with chronic diabetes. *Am J Physiol* **269**:H1288–H1296.

Watanabe M, Yokoshiki H, Mitsuyama H, Mizukami K, Ono T, and Tsutsui H (2012) Conduction and refractory disorders in the diabetic atrium. *Am J Physiol Heart Circ Physiol* **303**:H86–H95.

Willemsen S, Hartog JW, van Veldhuisen DJ, van der Meer P, Roze JF, Jaarsma T, Schalkwijk C,

van der Horst IC, Hillege HL, Voors AA (2012) The role of advanced glycation end-products and their receptor on outcome in heart failure patients with preserved and reduced ejection fraction. *Am Heart J* **164**:742.e3-749.e3.

Wu MS, Liang JT, Lin YD, Wu ET, Tseng YZ, and Chang KC (2008) Aminoguanidine prevents the impairment of cardiac pumping mechanics in rats with streptozotocin and nicotinamide-induced type 2 diabetes. *Br J Pharmacol* **154**:758–764.

Yamagishi S, Nakamura K, Matsui T, Ueda S, Noda Y, and Imaizumi T (2008) Inhibitors of advanced glycation end products (AGEs): potential utility for the treatment of cardiovascular disease. *Cardiovasc Ther* **26**:50–58.

Yang Z, Shen W, Rottman JN, Wikswo JP, Murray KT (2005) Rapid stimulation causes electrical remodeling in cultured atrial myocytes. *J Mol Cell Cardiol* **38**:299-308.

Yaras N, Ugur M, Ozdemir S, Gurdal H, Purali N, Lacampagne A, Vassort G, and Turan B (2005) Effects of diabetes on ryanodine receptor Ca release channel (RyR2) and $Ca^{2+}$ homeostasis in rat heart. *Diabetes* **54**:3082–3088.

Yeh YH, Hsu LA, Chen YH, Kuo CT, Chang GJ, and Chen WJ (2016) Protective role of hemeoxygenase-1 in atrial remodeling. *Basic Res Cardiol* **111**:58.

Yuan Q, Zhan L, Zhou QY, Zhang LL, Chen XM, Hu XM, and Yuan XC (2015) SIRT2 regulates microtubule stabilization in diabetic cardiomyopathy. *Eur J Pharmacol* **764**:554–561.

Zhang L, Cannell MB, Phillips AR, Cooper GJ, and Ward ML (2008) Altered calcium homeostasis does not explain the contractile deficit of diabetic cardiomyopathy. *Diabetes* **57**:2158–2166.

Zhong Y, Ahmed S, Grupp IL, and Matlib MA (2001) Altered SR protein expression associated with contractile dysfunction in diabetic rat hearts. *Am J Physiol Heart Circ Physiol* **281**:H1137–H1147.

## Footnotes.

This work was supported by the Chang Gung Medical Research Foundation [CMRPD170501~3 and BMRP468]; and the Ministry of Science and Technology of Taiwan [NSC96-2320-B-182-026-MY3 and NSC99-2320-B-182-005-MY3].

**Address correspondence to:** Gwo-Jyh Chang, Graduate Institute of Clinical Medicinal Sciences, College of Medicine, Chang Gung University, 259 Wen-Hwa 1st Road, Kwei-Shan, Tao-Yuan, Taiwan. E mail: **gjchang@mail.cgu.edu.tw**

# Legends for figures

**Fig. 1.** *In vivo* left ventricular (LV) performance and ECG recordings in anaesthetized rats and *ex vivo* conduction electrogram recordings in isolated hearts. (A) Representative traces of LV pressure (LVP), the first derivative of LVP (d*P*/d*t*), and lead II ECG recorded from control (Con) and diabetic (DM) rats with vehicle (Veh) or AG treatment. (B) Representative His bundle (HBE) and ventricular (VE) electrograms of Langendorff-perfused hearts from various groups. Electrograms were recorded at an atrial pacing cycle length of 200 ms. A, atrial depolarization; H, His bundle depolarization; S, stimulation artifact; T, ventricular repolarization; V, ventricular depolarization.

**Fig. 2.** Susceptibility to atrial and ventricular tachyarrhythmias in Langendorff-perfused hearts from control (Con) and diabetic (DM) rats with vehicle (Veh) or AG treatment. (A–C) Susceptibility to atrial tachyarrhythmias (AT). (A) Representative electrograms from control and diabetic groups treated with vehicle or AG following 1-s burst atrial pacing at a basic pacing cycle length of 200 ms. (B and C) Summary data of duration of AT and inter-atrial conduction time (IACT), respectively. The number of hearts in each group is indicated in parentheses. (D and E) Susceptibility to ventricular tachyarrhythmias (VT). (D) Examples of epicardial electrograms showing the severity of VT in different groups. Polymorphic ventricular tachycardia could be induced by one extra-stimulus ($S_1S_2$ of 30 ms) in the heart from a diabetic rat, whereas more extra-stimuli ($S_2$–$S_4$) failed to induce arrhythmia in the hearts from Con+Veh, Con+AG, and DM+AG group. $S_1S_2$, $S_2S_3$, and $S_3S_4$ interval all of 30 ms. (E) Inducibility quotient of ventricular tachyarrhythmias in various groups. Values are means ± SEM. **P* < 0.05 and ***P* < 0.01 vs. Con+Veh group. †*P* < 0.05 and ‡*P* < 0.01 vs. DM+Veh group.

**Fig. 3.** Rate-dependence of action potential (AP) recorded in left ventricular papillary muscles from control (Con) and diabetic (DM) rats with vehicle (Veh) or AG treatment. (A) Representative AP

traces recorded at 1 and 4 Hz from various groups. (B) Effects of increased stimulus frequency (0.5–4 Hz) on AP duration (APD) at 25%, 50% and 90% repolarization levels, AP amplitude, maximal depolarization velocity ($V_{max}$), or resting membrane potential (RMP) in various groups. Values are means ± SEM. *$P$ < 0.05, **$P$<0.01, and #$P$ < 0.001 vs. Con+Veh group. †$P$ < 0.05, ‡$P$ < 0.01 and \$$P$ < 0.001 vs. DM+Veh group.

**Fig. 4.** Intracellular $Ca^{2+}$ transients and contractile properties of LV myocytes isolated from hearts of various groups. (A) Representative $Ca^{2+}$ transients (fura-2 fluorescence ratio $F_{340}/F_{380}$, upper panel) with fitted curves and cell-shortening (lower panel) traces recorded during field stimulation at 1 Hz. (B and C) Intracellular $Ca^{2+}$ transient (B) and contraction (C) properties of myocytes isolated from Con+Veh ($n$ = 40 myocytes/5 rats), DM+Veh ($n$ = 52/8), Con+AG ($n$ = 53/7) and DM+AG ($n$ = 39/7) groups. Values are means ± SEM. *$P$ < 0.05, **$P$ < 0.01, and #$P$ < 0.001 vs. Con+Veh group. †$P$ < 0.05, ‡$P$ < 0.01 and \$$P$ < 0.001 vs. DM+Veh group.

**Fig. 5.** Caffeine-induced Intracellular $Ca^{2+}$ transients of LV myocytes isolated from hearts of various groups. (A) Representative tracings of caffeine-induced $Ca^{2+}$ transients. Myocytes were first stimulated at 1 Hz and caffeine (10 mM) was rapidly applied 10 s after cessation of electrical stimulation. (B and C) Bar graphs showing the averaged data of the amplitude and decay time constant (τ) of the caffeine-induced $Ca^{2+}$ transients in myocytes from Con+Veh ($n$ = 24 myocyte/5 rats), DM+Veh ($n$ = 29/7), Con+AG ($n$ = 33/7) and DM+AG ($n$ = 23/6) groups. Values are means ± SEM. #$P$ < 0.001 vs. Con+Veh group. †$P$<0.05 vs. DM+Veh group.

**Fig. 6.** Western blot analysis of SERCA2a (A), PLB (B), $pSer^{16}$-PLB (C), RyR2 (D), NCX (E), and AGE (F) expression in LV tissues from control and diabetic rats treated with vehicle or AG. The same blot of each target protein was probed with GAPDH antibody as an internal control. Bars represent means ± SEM of 14, 14, 14, 13, 11 and 10 hearts in each group for the study of SERCA2a, PLB,

pSer$^{16}$-PLB, RyR2, NCX, and AGEs respectively. All measurements were normalized to the protein levels of GAPDH in each blot. #$P < 0.001$ vs. Con+Veh group. ‡$P < 0.01$ and \$$P < 0.001$ vs. DM+Veh group.

**Fig. 7.** Effects of AG on high glucose (HG)-induced AGEs formation and ROS production (A-B) and effects of RAGE knockdown on HG-induced ROS production (C-D) in HL-1 cells. (A and B): (A) Western blot analysis of AGE expression in myocytes incubated with normal (NG, 5.6 mM), high glucose (HG, 25 mM), or mannitol (Man; 19.4 mM mannitol with 5.6 mM glucose, the osmotic control) for 24 h and subsequent treatment with vehicle or 1 μM AG for the last 12 h. The same blot of the target protein was probed with tubulin antibody as an internal control. All measurements were normalized to the levels of tubulin in each blot. The relative expression level was normalized to that of NG+vehicle group. Each value represents the means ± SEM of five independent experiments. (B) Intracellular ROS production was measured by DCF-DA (cytoplasm staining) or DHE (nucleus staining) fluorescent dye using confocal microscope (left panel) in cells treated with the identical conditions as in panel (A) Relative fluorescence density was quantified (right panel). Each value represents the means ± SEM of five independent experiments. *$P$<0.05, **$P < 0.01$, and #$P < 0.001$ vs. NG+Veh group. †$P < 0.05$ and \$$P < 0.001$ vs. HG+Veh group. (C and D): (C) After transfected with indicated siRNA for 48 h, cells were incubated with HG for 24 h and subsequent treatment with vehicle or 1 μM AG for the last 12 h, the expression of RAGE and tubulin was evaluated by Western blotting (upper panel). The relative expression level was normalized to the level of control siRNA (Con si) group. Bars represent means ± SEM of five independent experiments in each group. (D) Intracellular ROS production was measured by DCF-DA or DHE (left panel) in cells with conditions as in panel C. Relative fluorescence density was quantified (right panel). Each value represents the means ± SEM of five independent experiments. *$P$<0.05, **$P < 0.01$, and #$P$<0.001 vs. HG+Con si group. ‡$P < 0.01$ vs. HG+RAGE si group.

**Fig. 8.** Effects of AG on high glucose (HG)-induced AP remodeling (A-B) and effects of RAGE knockdown on HG-induced AP remodeling (C-D) in HL-1 cells. Cells were treated as the same conditions shown in Fig. 7. (A and B): (A) Representative AP traces recorded at 1 Hz from cells incubated with normal glucose (NG, 5.6 mM glucose), HG (25 mM glucose) or mannitol (Man, 19.4 mM mannitol with 5.6 mM glucose) with vehicle (Veh) or AG (1 μM) treatment. (B) Averaged AP duration (APD) at 50% and 90% repolarization levels in various groups. Bars represent means ± SEM of 8 cells in each group. **P*<0.05 and #*P* < 0.001 vs. NG+Veh group. †*P* < 0.05 and ‡*P* < 0.01 vs. HG+Veh group. (C and D): (C) Representative AP traces recorded at 1 Hz in control (Con si) or RAGE knockdown (RAGEsi) cells incubated with HG with or without AG treatment. (D) Averaged APD at 50% and 90% repolarization levels in various groups. Bars represent means ± SEM of 8 cells in each group. **P*<0.05, ***P* < 0.01, and #*P*<0.001 vs. HG+Con si group.

**Fig 9.** Whole-cell $K^+$ currents recorded in LV myocytes from control and diabetic rats treated with vehicle or AG. (A) Representative normalized $K^+$ current traces in myocytes from Con+Veh (227 pF), Con+AG (236 pF), DM+Veh (223 pF), and DM+AG (165 pF) rats. (B) Average current density–voltage (*I–V*) relationships of $I_{to}$ and $I_{K1}$ peak currents. $I_{to}$ was measured as the difference between the peak current and the steady-state current at the end of the pulse. (C) Average *I–V* relationships of $I_{SS}$ current. $I_{SS}$ was measured as the steady-state current at the end of the pulse. (D) Voltage-dependent decay kinetics of $I_{to}$ from various groups. Data were obtained by fitting with a monoexponential function. (E and F) Steady-state activation (E) and inactivation (F) curves of $I_{to}$ in LV myocytes from various groups. The activation curves were derived using *I–V* curves shown in panel B. Steady-state inactivation was examined with a double-pulse protocol (inset). The relative peak amplitudes of $I_{to}$ were plotted against prepulse potentials. Smooth lines represent the fit of a Boltzmann function to the data. (G) Fractional recovery ($I_{\text{test pulse}}/I_{\text{prepulse}}$) of $I_{to}$ from inactivation plotted as a function of recovery time in myocytes from various groups. Recovery of $I_{to}$ was determined with the paired-pulse protocol as shown in the inset. Smooth lines represent the fit of a

monoexponential function to the data. Data are means ± SEM. ***P* < 0.01 and #*P* < 0.001 vs. Con+Veh group. †*P* < 0.05 vs. DM+Veh group.

JPET Fast Forward. Published on October 31, 2018 as DOI: 10.1124/jpet.118.252080
This article has not been copyedited and formatted. The final version may differ from this version.



TABLE 1

General characteristics, hemodynamic and electrocardiogram variables in control (Con) and diabetic (DM) rats treated with vehicle (Veh) or aminoguanidine (AG)

| | Con+Veh | DM+Veh | Con+AG | DM+AG |
|---|---|---|---|---|
| Sample size (*n*) | 16 | 18 | 15 | 22 |
| Initial BW (g) | 211.9 ± 5.2 | 205.8 ± 5.1 | 208.7 ± 4.2 | 209.8 ± 3.4 |
| Final BW (g) | 380.3 ± 14.1 | 216.1 ± 8.6# | 384.3 ± 13.4 | 226.8 ± 9.7# |
| HW (g) | 1.33 ± 0.06 | 0.93 ± 0.04# | 1.38 ± 0.05 | 0.90 ± 0.04# |
| AW (g) | 0.17 ± 0.01 | 0.15 ± 0.01 | 0.18 ± 0.01 | 0.14 ± 0.01 |
| LVW (g) | 0.67 ± 0.03 | 0.45 ± 0.02# | 0.66 ± 0.02 | 0.42 ± 0.02# |
| HW/BW (mg/g) | 3.49 ± 0.08 | 4.34 ± 0.12# | 3.62 ± 0.11 | 3.98 ± 0.08**† |
| AW/BW (mg/g) | 0.44 ± 0.01 | 0.70 ± 0.03# | 0.47 ± 0.02 | 0.61 ± 0.03#† |
| LVW/BW (mg/g) | 1.76 ± 0.06 | 2.11 ± 0.08** | 1.73 ± 0.07 | 1.87 ± 0.04† |
| Blood glucose (mg/dL) | 164.1 ± 12.1 | 455.6 ± 19.3# | 152.0 ± 16.2 | 399.0 ± 25.3# |
| Sample size (*n*) | 24 | 27 | 24 | 26 |
| HR (beats/min) | 325 ± 12 | 265 ± 9# | 324 ± 11 | 274 ± 7** |
| MAP (mmHg) | 70.4 ± 2.4 | 71.2 ± 3.2 | 70.2 ± 2.3 | 72.2 ± 3.0 |
| LVESP (mmHg) | 118.1 ± 2.7 | 99.1 ± 2.1# | 118.5 ± 2.2 | 107.9 ± 2.2*† |
| LVEDP (mmHg) | 4.6 ± 0.7 | 7.1 ± 0.6* | 5.2 ± 0.6 | 5.7 ± 0.7 |
| LVDP (mmHg) | 113.5 ± 2.7 | 92.3 ± 2.5# | 113.2 ± 2.3 | 102.2 ± 2.1**† |
| d$P$/d$t_{max}$ (mmHg/s) | 7445 ± 461 | 5782 ± 395* | 8045 ± 409 | 6608 ± 357 |
| d$P$/d$t_{min}$ (mmHg/s) | 5573 ± 363 | 3939 ± 256# | 5075 ± 277 | 4606 ± 191 |
| Tau (ms) | 11.1 ± 0.7 | 16.3 ± 0.4# | 11.8 ± 0.8 | 13.7 ± 0.4*‡ |
| PR (ms) | 60.6 ± 2.0 | 59.9 ± 2.1 | 61.2 ± 1.7 | 59.3 ± 1.6 |
| QRS (ms) | 15.3 ± 0.4 | 15.3 ± 0.5 | 15.0 ± 0.3 | 14.8 ± 0.3 |
| QTc (ms) | 214.8 ± 4.5 | 253.4 ± 10.2** | 212.7 ± 5.2 | 224.6 ± 4.2† |

Data are expressed as means ± SEM. "Initial" and "final" represent the observation times of the beginning of first week and the end of the sixth week of the experimental period, respectively. AW indicates atrial weight; BW; body weight; HW, heart weight; LVW, left ventricular weight; HR, heart rate; MAP, mean arterial pressure; LVESP, LV end-systolic pressure; LVEDP, LV end-diastolic pressure; LVDP, LV developed pressure; d$P$/d$t_{max}$ and d$P$/d$t_{min}$, maximal rate of rise and fall of LV pressure. Tau, time constant of LV pressure decay; Rate-corrected QT intervals (QTc) were derived using the Bazett's formula QTc (ms) = measured QT interval (ms)/[square root of RR interval (s)].

*$P$<0.05, **$P$<0.01 and #$P$<0.001 vs. Con+Veh group. †$P$<0.05 and ‡$P$<0.01 vs. DM+Veh group.

TABLE 2

Conduction system parameters recorded from the isolated perfused hearts of control (Con) and diabetic (DM) rats treated with vehicle or AG

| | Con+Veh ($n$ = 21) | DM+Veh ($n$ = 24) | Con+AG ($n$ = 21) | DM+AG ($n$ = 24) |
|---|---|---|---|---|
| BCL | 243.3 ± 5.9 | 269.2 ± 8.6* | 241.4 ± 6.6 | 255.6 ± 5.6 |
| SA | 10.5 ± 0.3 | 10.9 ± 0.4 | 9.9 ± 0.4 | 10.5 ± 0.4 |
| AH | 25.7 ± 1.0 | 25.0 ± 0.7 | 23.7 ± 0.8 | 26.1 ± 1.0 |
| HV | 19.5 ± 0.8 | 18.6 ± 1.0 | 18.9 ± 0.5 | 19.5 ± 0.8 |
| QT | 42.1 ± 3.5 | 54.0 ± 3.0* | 43.3 ± 2,4 | 45.0 ± 2.1† |
| WCL | 114.8 ± 3.3 | 123.8 ± 3.3 | 113.3 ± 2.6 | 118.8 ± 2.2 |
| AERP | 38.6 ± 1.7 | 48.8 ± 2.0** | 40.0 ± 2.7 | 41.3 ± 1.5† |
| AVNERP | 88.6 ± 2.6 | 103.8 ± 2.8# | 90.5 ± 2.6 | 96.7 ± 2.0* |
| HPFRP | 117.6 ± 2.4 | 134.2 ± 2.7# | 121.0 ± 4.0 | 126.9 ± 1.7** |
| VERP | 40.0 ± 4.1 | 58.8 ± 3.1** | 44.8 ± 3.8 | 46.7 ± 2.2† |

Data (in ms) are expressed as means ± SEM. BCL, basic cycle length; SA, stimulus-atrial conduction interval; AH, atrio-His bundle conduction interval; HV, His-ventricular conduction interval; WCL, Wenckebach cycle length; AERP, atrial effective refractory period; AVNERP, AV nodal effective refractory period; HPFRP, His-Purkinje system functional refractory period; VERP, ventricular effective refractory period. The QT interval (interval between V and T wave) was used as the parameter for monitoring ventricular repolarization. SA, AH, HV, and QT intervals were recorded at a pacing cycle length of 200 ms.

*$P$<0.05, **$P$<0.01, and #$P$<0.001 vs. Con+Veh group. †$P$<0.05 vs. DM+Veh group.

JPET Fast Forward. Published on October 31, 2018 as DOI: 10.1124/jpet.118.252080
This article has not been copyedited and formatted. The final version may differ from this version.



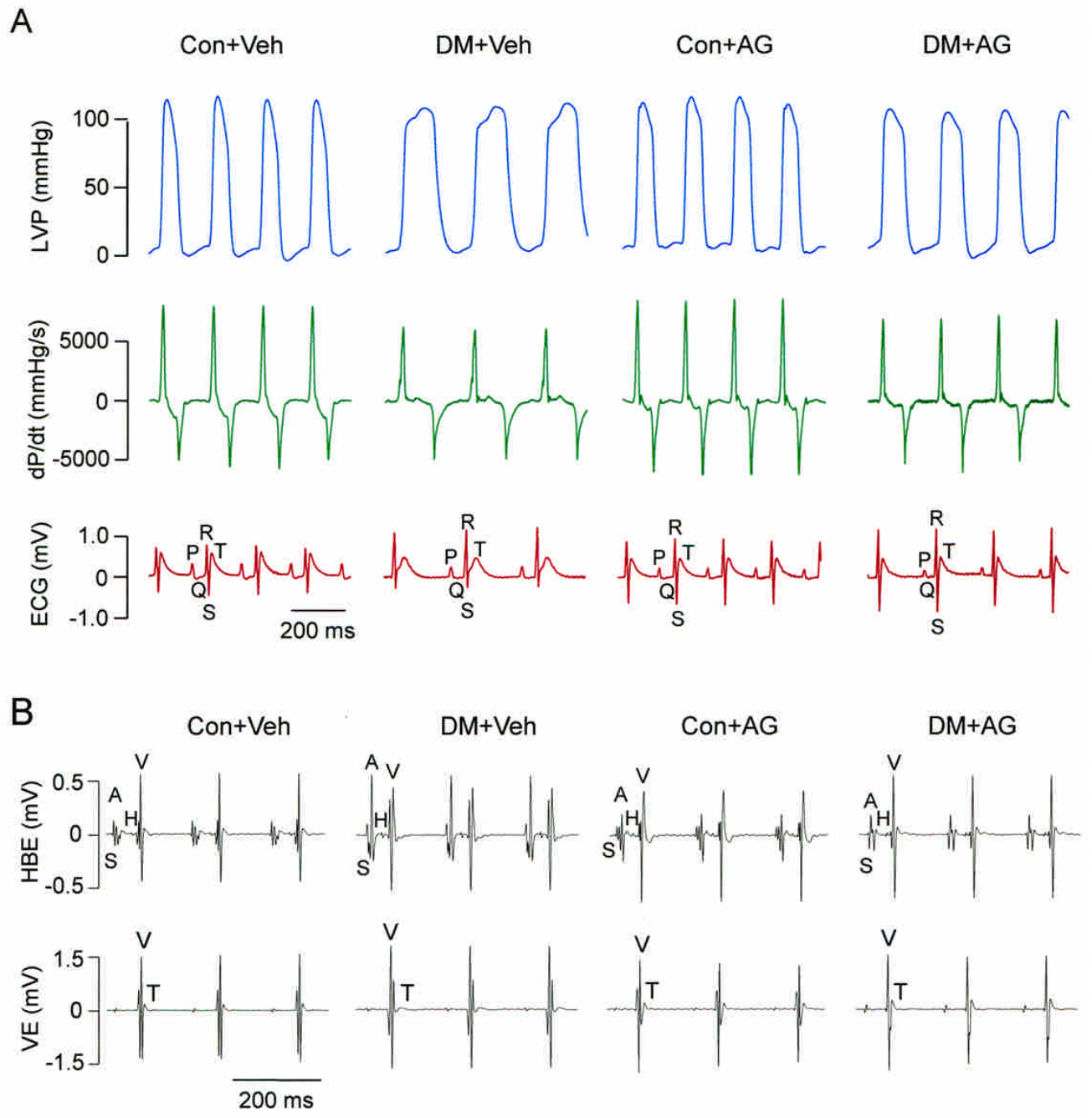


**Figure 1**

JPET Fast Forward. Published on October 31, 2018 as DOI: 10.1124/jpet.118.252080
This article has not been copyedited and formatted. The final version may differ from this version.



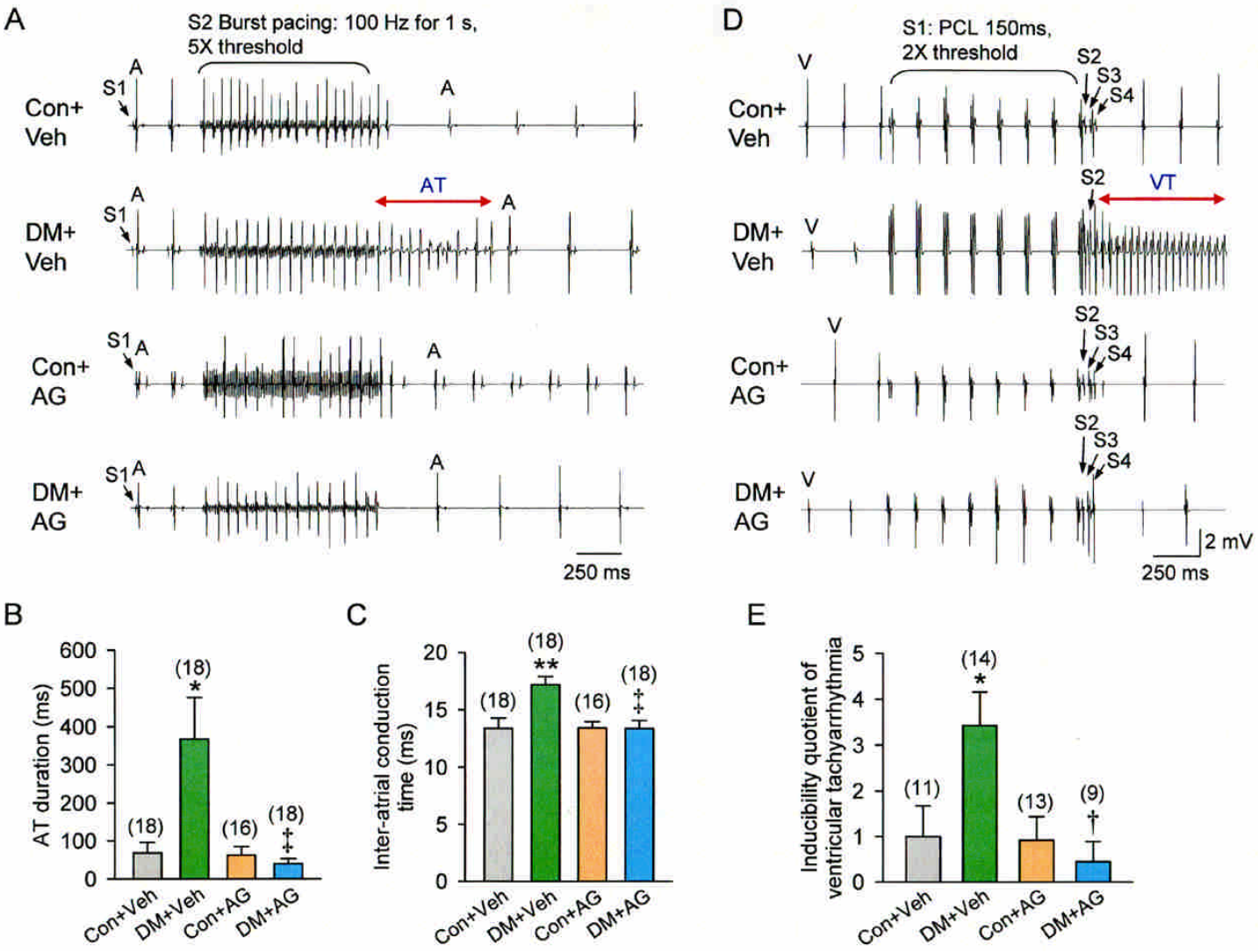


**Figure 2**

JPET Fast Forward. Published on October 31, 2018 as DOI: 10.1124/jpet.118.252080
This article has not been copyedited and formatted. The final version may differ from this version.



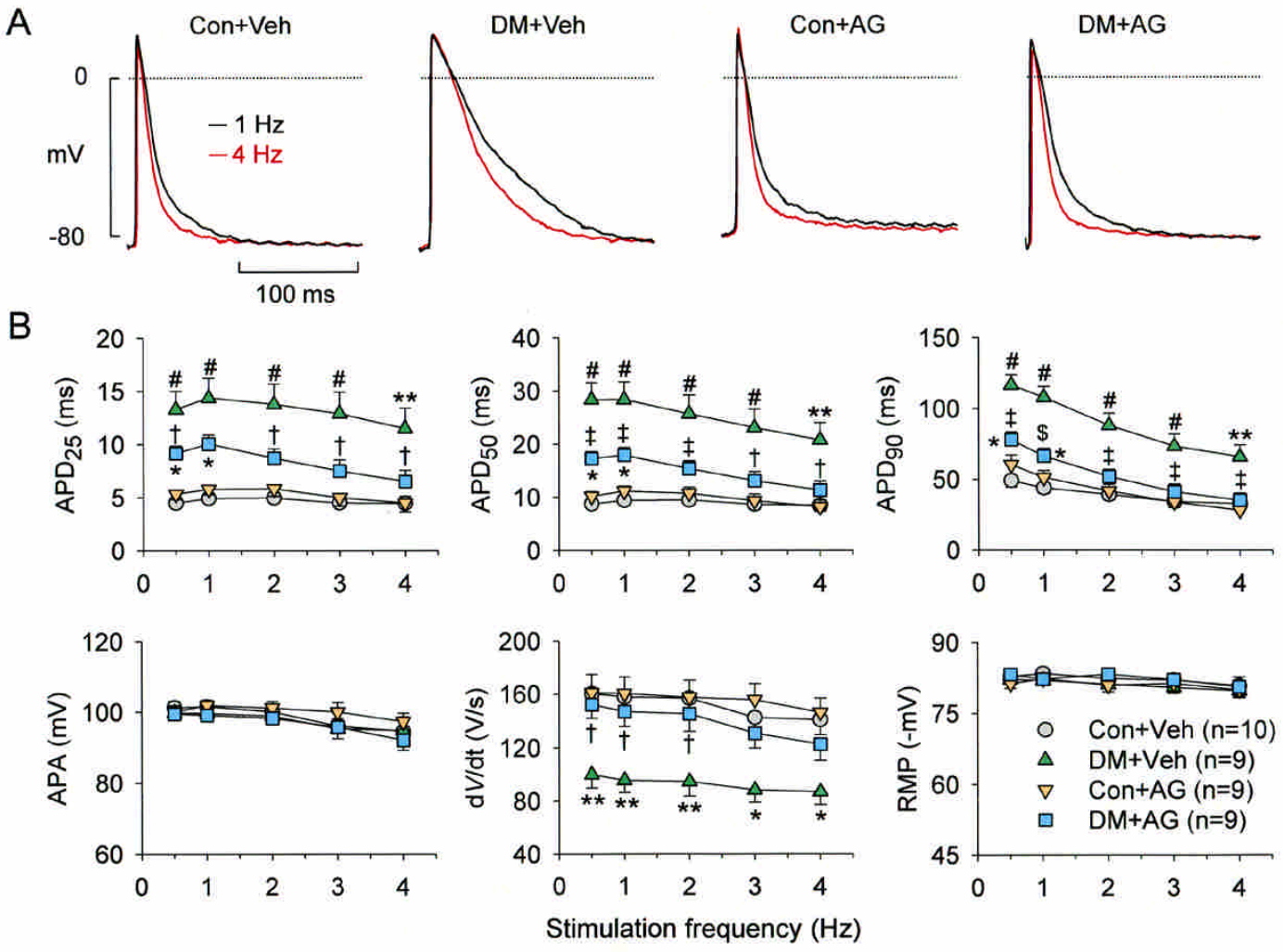


**Figure 3**

JPET Fast Forward. Published on October 31, 2018 as DOI: 10.1124/jpet.118.252080
This article has not been copyedited and formatted. The final version may differ from this version.



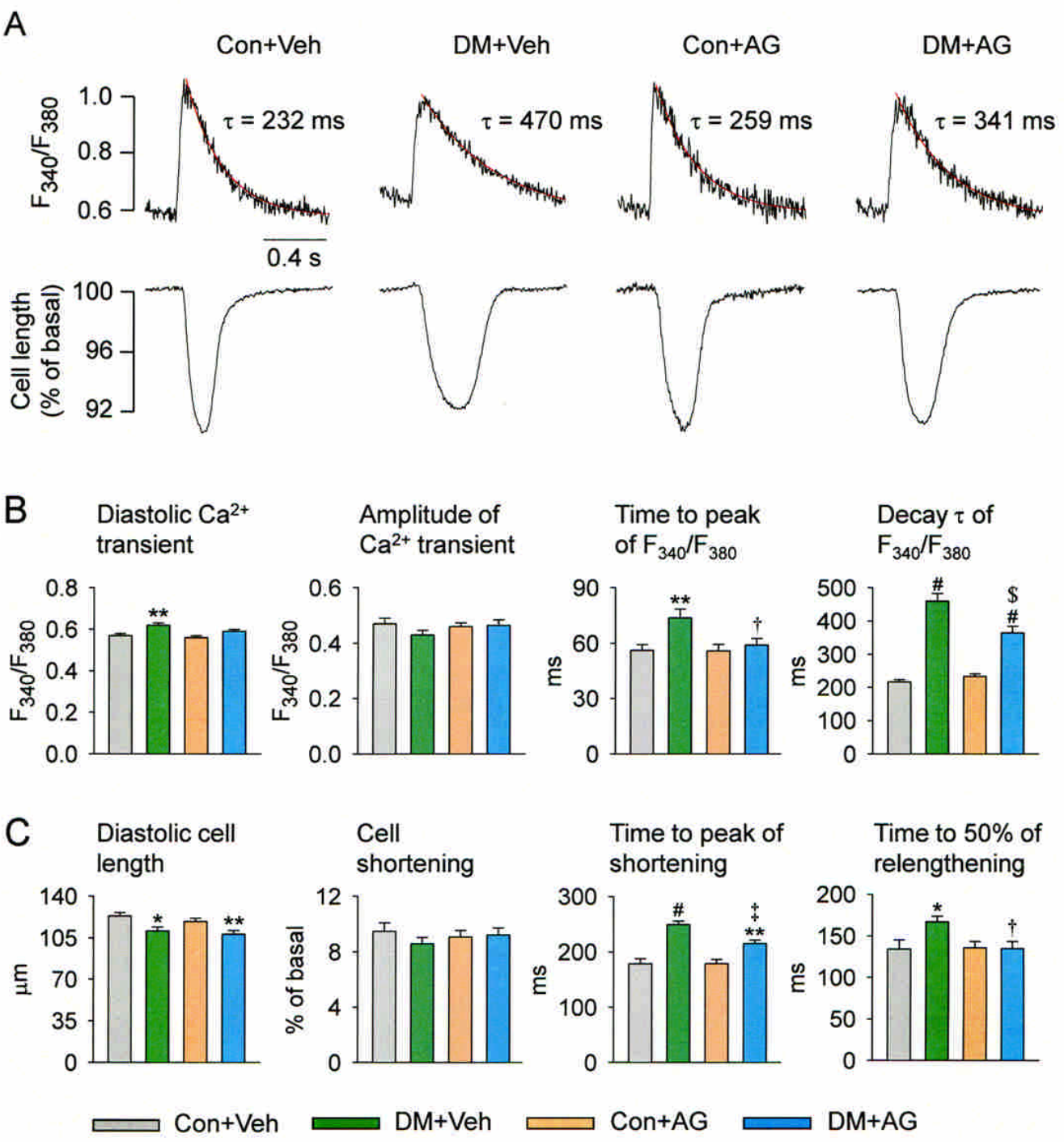


**Figure 4**

JPET Fast Forward. Published on October 31, 2018 as DOI: 10.1124/jpet.118.252080
This article has not been copyedited and formatted. The final version may differ from this version.



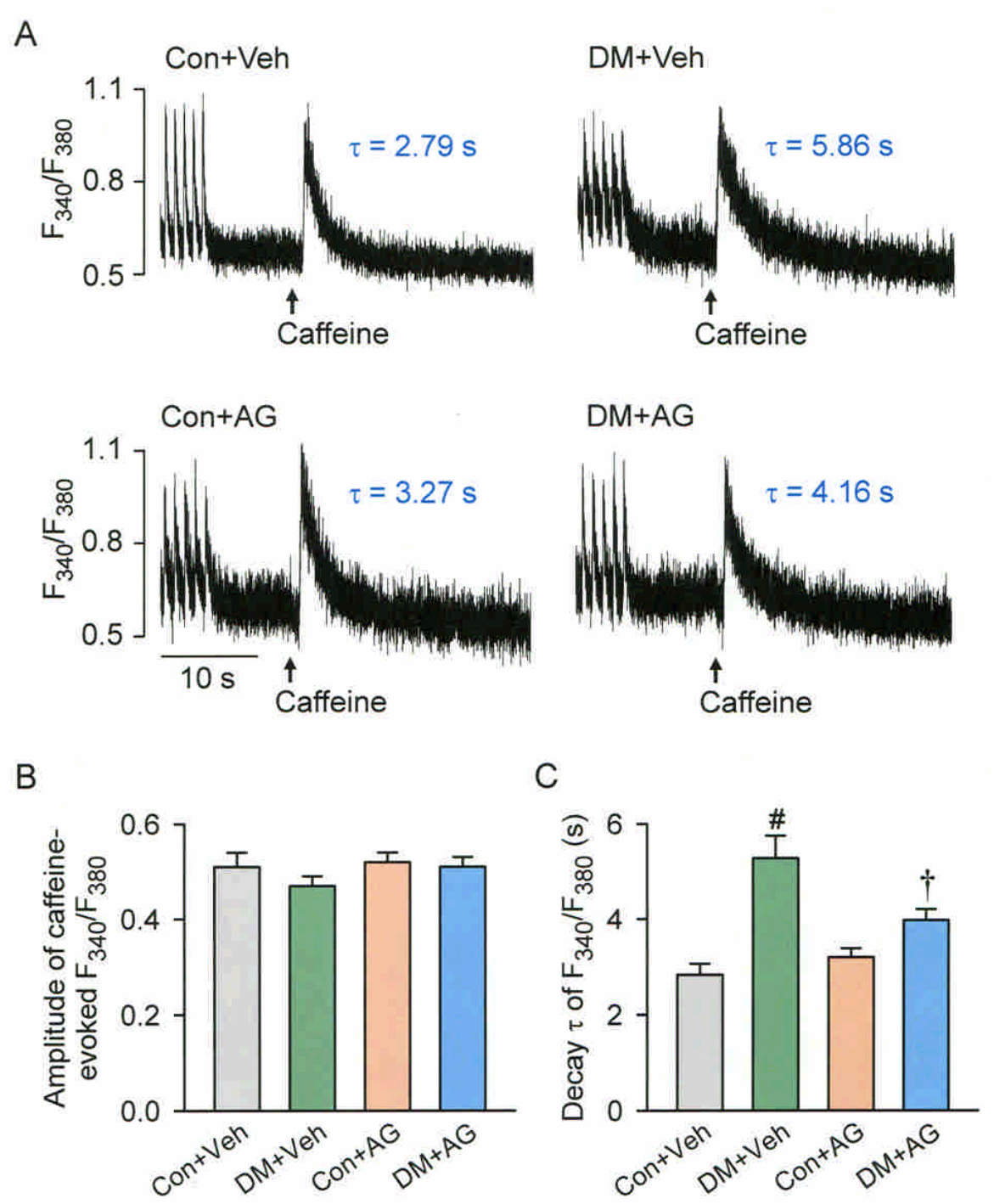


**Figure 5**

JPET Fast Forward. Published on October 31, 2018 as DOI: 10.1124/jpet.118.252080
This article has not been copyedited and formatted. The final version may differ from this version.



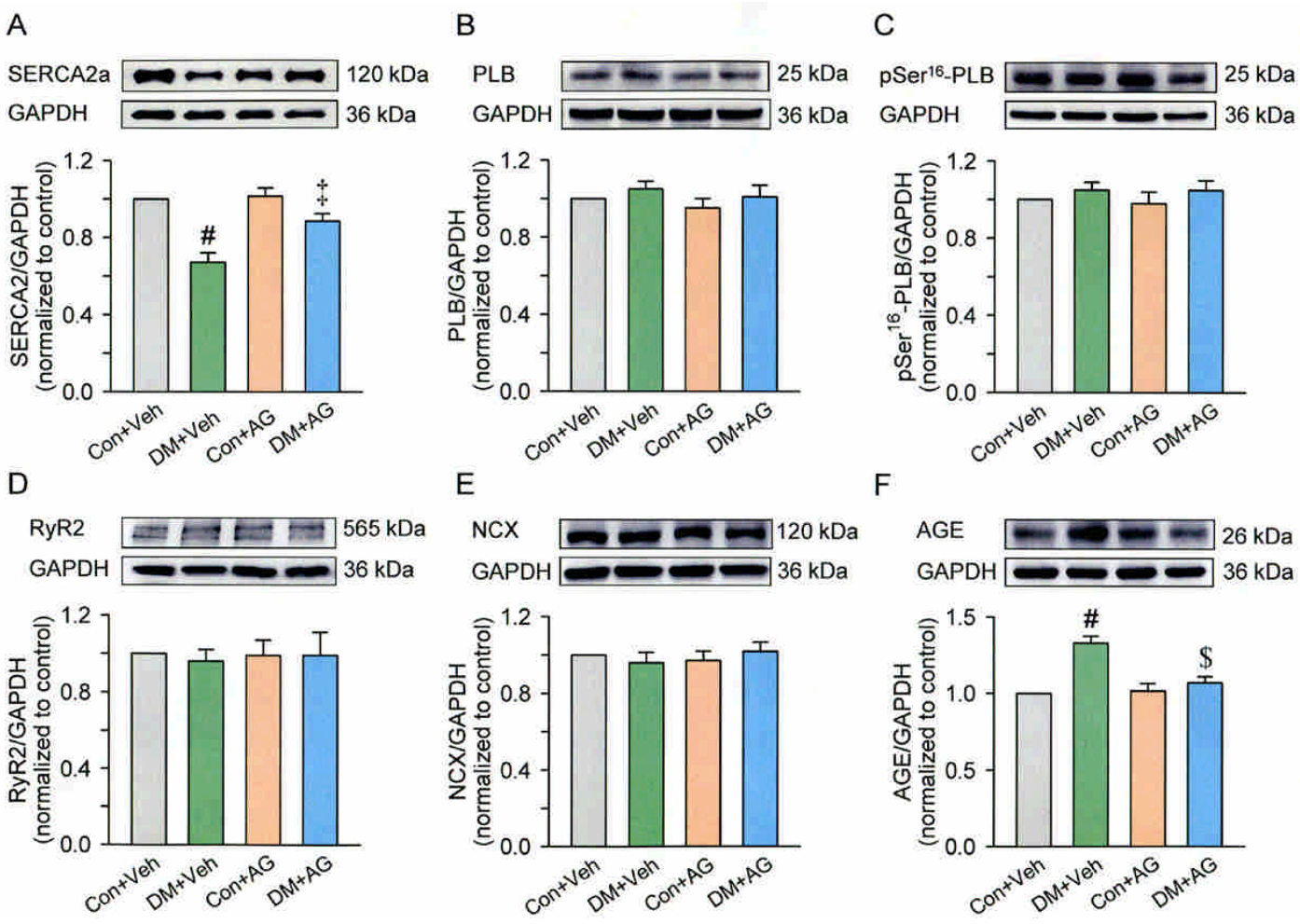


**Figure 6**

JPET Fast Forward. Published on October 31, 2018 as DOI: 10.1124/jpet.118.252080
This article has not been copyedited and formatted. The final version may differ from this version.



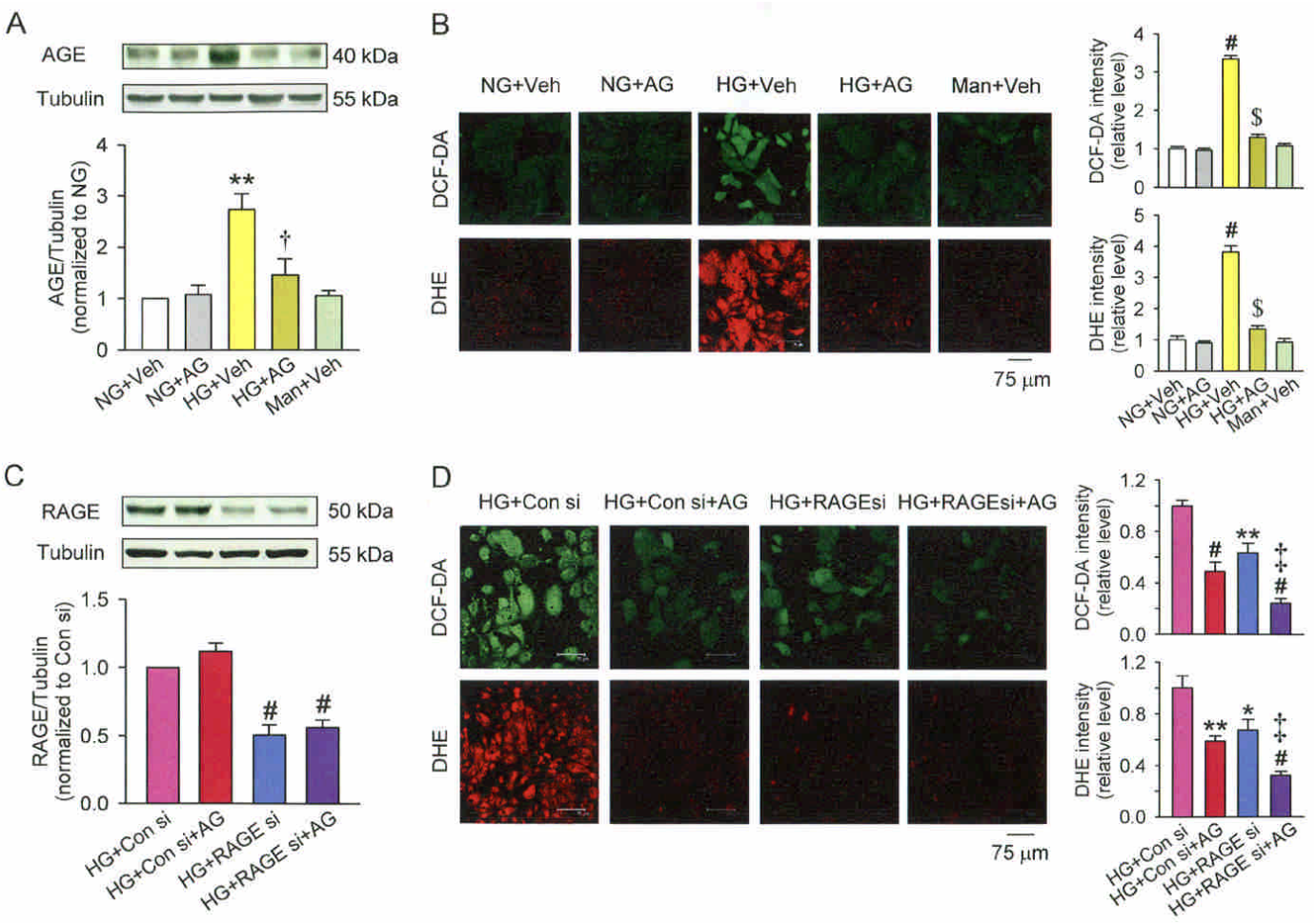


**Figure 7**

JPET Fast Forward. Published on October 31, 2018 as DOI: 10.1124/jpet.118.252080
This article has not been copyedited and formatted. The final version may differ from this version.



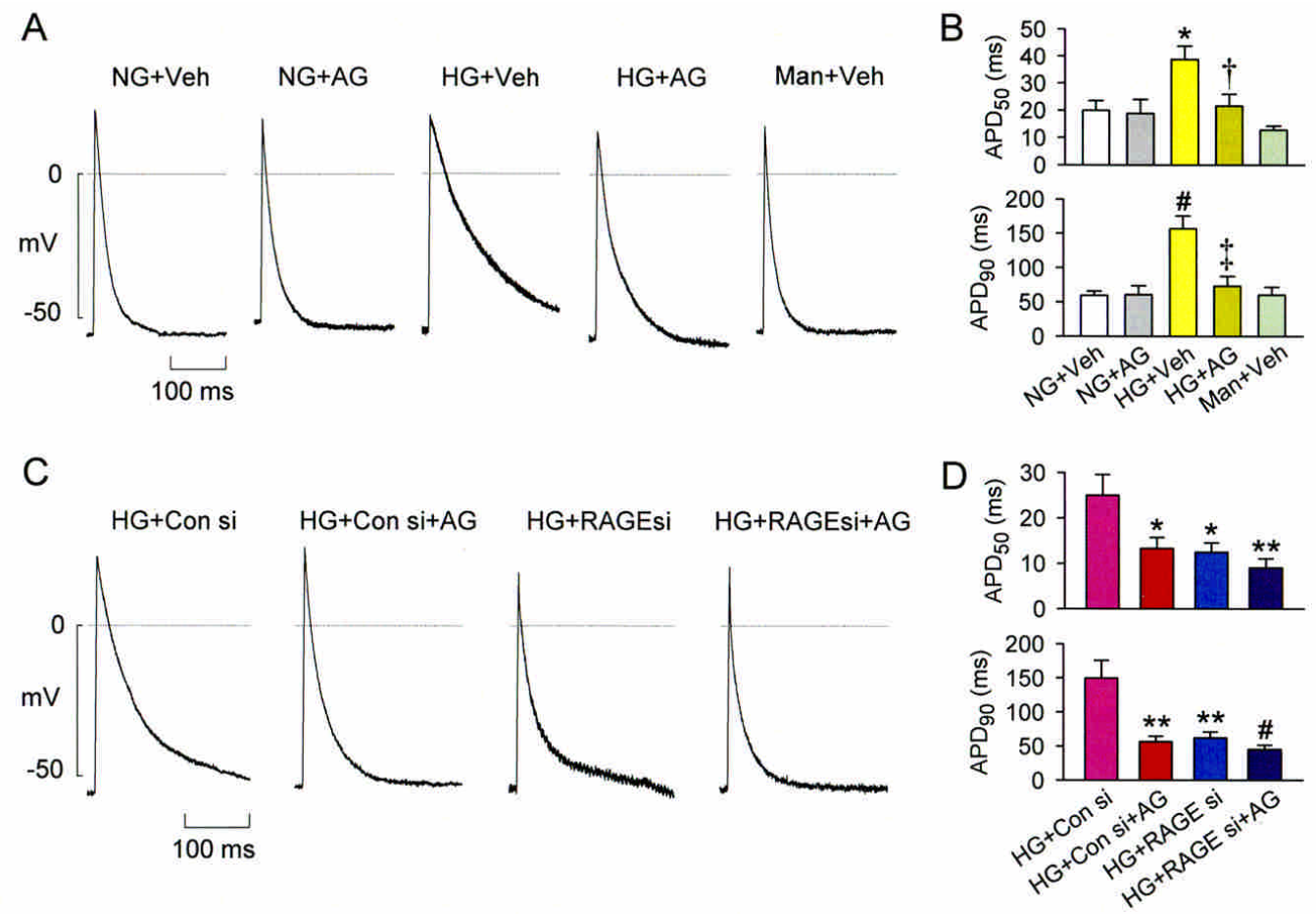


**Figure 8**

JPET Fast Forward. Published on October 31, 2018 as DOI: 10.1124/jpet.118.252080
This article has not been copyedited and formatted. The final version may differ from this version.



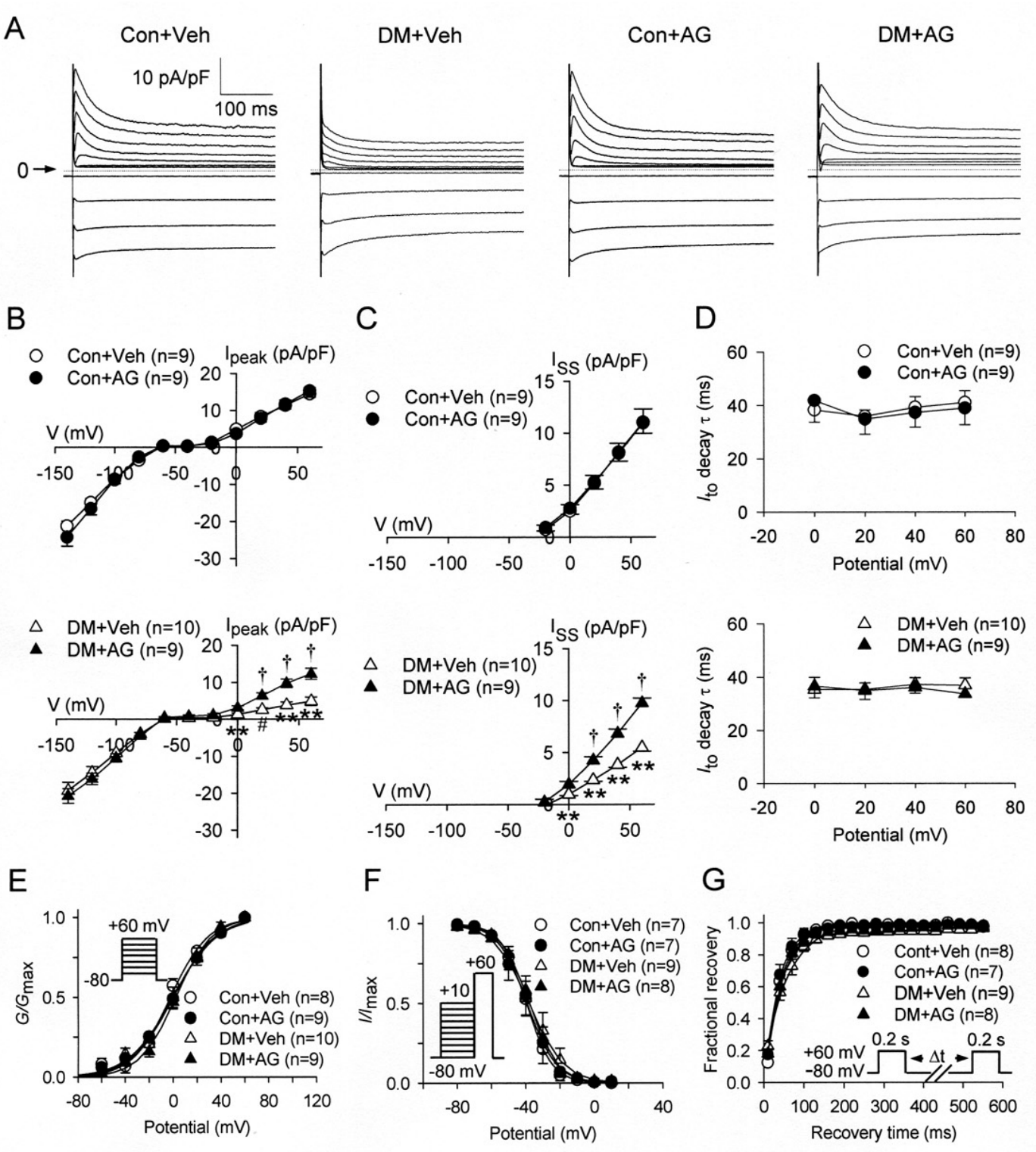


**Figure 9**

# Supplemental Material

## Inhibition of advanced glycation end products formation attenuates cardiac electrical and mechanical remodeling and vulnerability to tachyarrhythmias in diabetic rats

Gwo-Jyh Chang, Yung-Hsin Yeh, Wei-Jan Chen, Yu-Shien Ko, Jong-Hwei S. Pang and Hsiao-Yu Lee

## Expanded Methods

### Atrial tachyarrhythmia vulnerability

Following the intracardiac conduction recording study, a bipolar platinum electrode was placed on the left atrium to record the atrial electrogram, while the other one was placed on the apex to record ventricular signals. Pacing current was delivered via a bipolar electrode placed on the right atrium (RA) appendage. The inter-atrial conduction time (IACT) was defined as the time from the RA appendage pacing spike to the left atrium (LA) appendage activation at a pacing cycle length of 200 ms. Atrial tachyarrhythmia (AT) was induced with burst pacing after 8 regularly paced stimuli ($S_1$) at 200-ms pacing cycle length (PCL) and 5× diastolic threshold. The burst pacing current ($S_2$) was consisted of a train of 100 square wave pulses, 1 ms in duration at a frequency of 100 Hz for a duration of 1 s. The duration of AT was defined as a period of rapid irregular atrial rhythm deviating from sinus rhythm for > 0.1 s. The mean duration of AT in each heart was determined on the basis of 5 inductions.

### Ventricular tachyarrhythmia vulnerability

After isolaton, the heart was mounted on a Langendorff perfusion apparatus, and perfused with oxygenated (95% $O_2$ and 5% $CO_2$) modified Tyrode's solution containing (in mM): 117 NaCl, 4.6 KCl, 1.0 $MgCl_2$, 23 $NaHCO_3$, 0.8 $NaH_2PO_4$, 2 $CaCl_2$ and 5.5 dextrose, equilibrated at 37°C. Ventricular epicardial electrograms were recorded by a bipolar electrode, placed on the epicardial surface of the LV apex. A bipolar pacing electrode was placed on the anterior epicardial surface of the right ventricle. Induction of ventricular arrhythmias was then attempted by programmed electrical stimulation at a PCL of 150 ms ($S_1$) with one to three ($S_2$, $S_3$, and $S_4$) extrastimuli delivered after 8 paced beats. Stimulation intensity was twice the threshold and 5 ms in duration. Pacing protocols were interrupted if sustained ventricular tachyarrhythmia was induced. The end point of testing was the induction of nondriven ventricular

tachyarrhythmia. A preparation was considered noninducible when ventricular pacing produced either no ventricular premature beats or only self-terminating salvos of < 6 beats. Ventricular tachyarrhythmias including ventricular tachycardia and fibrillation were considered nonsustained when it lasted ≤ 15 beats and sustained when it lasted > 15 beats. An arrhythmia scoring system was used as previously described (Nguyen et al., 1998): 0, noninducible preparations; 1, nonsustained tachyarrhythmias induced with 3 extrastimuli; 2, sustained tachyarrhythmias induced with 3 extrastimuli; 3, nonsustained tachyarrhythmias induced with 2 extrastimuli; 4, sustained tachyarrhythmias induced with 2 extrastimuli; 5, nonsustained tachyarrhythmias induced with 1 extrastimuli; 6, sustained tachyarrhythmias induced with 1 extrastimuli; and 7, tachyarrhythmias induced during the 8 paced beats at a PCL of 150 ms. If the heart stopped before the pacing, the arrhythmia score assigned to that heart was 8. When multiple forms of arrhythmias occurred in one heart, the highest score was used.

**Isolation of rat cardiomyocytes**

Single cardiomyocytes were isolated using a modification of the enzymatic dissociation procedure as described previously (Chang et al., 2014). After removal, the heart was perfused with 50 ml 1 mM $Ca^{2+}$-containing HEPES-buffered Tyrode's solution oxygenated with 100% $O_2$ and maintained at room temperature. Then the heart was mounted on a Langendorff apparatus, and perfused with nominally $Ca^{2+}$-free HEPES-buffered Tyrode's solution containing (mM): 137 NaCl, 5.4 KCl, 1.2 $KH_2PO_4$, 1.22 $MgSO_4$, 22 dextrose, 6 HEPES (pH adjusted to 7.4 with NaOH), supplemented with 20 mM taurine and maintained at 37°C. After 6 min. the perfusate was switched to the same solution supplemented with 0.4–0.5 $mg \cdot ml^{-1}$ collagenase (Type II; Worthington Biochem, USA) and 0.04 $mg \cdot ml^{-1}$ protease (Type XIV; Sigma-Aldrich, USA), additionally containing 0.01 mM $CaCl_2$. After 30 to 40-min digestion, the residual enzyme solution was removed by more than 5-min perfusion with $Ca^{2+}$-free HEPES-buffered solution supplemented with bovine serum albumin (1 mg/ml) and 0.05 mM $CaCl_2$. Thereafter, the atria and left ventricle were removed, cut into small pieces and mechanically agitated with a pipette in a 0.1 mM $Ca^{2+}$-containing buffer solution. The dispersed myocytes were then stored at room temperature in a 0.5 mM $Ca^{2+}$-containing solution for later use.

**Western blot analysis**

Equal amount of proteins were extracted from LV tissues or cultured HL-1 cells and subjected to electrophoresis on 4%–20% gradient gel (Mini-Protean® Precast gels, Bio-Rad, Hercules, CA, USA; for RyR2), 10% (SERCA2a or RAGE), 15% (PLB or phosphorylated $pSer^{16}$-PLB), 8% (NCX1), or 12% (AGE) SDS-PAGE in a minigel apparatus (Bio-Rad) and transferred to PVDF membranes (PerkinElmer Life Sciences, Boston, MA, USA). Membranes were blocked and then probed with

primary antibodies against RyR2 (1:1000; Thermo Fisher Scientific, MA, USA), SERCA2a (1:5000; Badrilla, Leeds, UK), PLB (1:2000; Badrilla), pSer$^{16}$-PLB (1:2000; Millipore, Temecula, CA, USA), NCX1 (1:500; Santa Cruz Biotech, CA, USA), AGE (1:600; TransGenic, Fukuoka, Japan), or RAGE (1:1000; Abcam, MA, USA) overnight at 4°C. The blot probed with GAPDH (1:1000; Santa Cruz) or tubulin antibody (1:1000; Santa Cruz) was used as an internal control. The membranes were then incubated with IgG antibody (Millipore) conjugated to horseradish peroxidase for 1 h at room temperature. The antibody-antigen complexes in all membranes were visualized using the enhanced chemiluminescence detection kit (PerkinElmer) and digitized in a BioSpectrum 500 Imaging System (UVP, Upland, CA, USA). The densities of the immunoreactive bands were analyzed using VisionWorks LS image software (verasion 6.6a, UVP).

**Whole-cell patch-clamp recording**

***Recording technique***

Ionic currents of LV or atrial myocytes were studied in whole-cell configuration at room temperature (25–27°C) as described previously (Chang et al., 2014). A small aliquot of the solution containing the isolated cardiomyocytes was placed in a 1 ml chamber mounted on the stage of an inverted microscope (Axio Observer Z1, Carl Zeiss). Cells were bathed in 1.8 mM $Ca^{2+}$ HEPES-buffered Tyrode's solution. Patch electrodes were fabricated from glass capillaries (o.d.: 1.5 mm, i.d. 1.0 mm; A-M Systems, Carlsborg, WA, USA) and fire-polished to give a pipette resistance of 2–5 MΩ when filled with the pipette solution and immersed in the external solution. Membrane currents were recorded in the voltage-clamp mode using an integrating patch-clamp amplifier (Axopatch 200B, Molecular Devices, CA, USA). Action potentials of single HL-1 cells were recorded in the current-clamp mode at a rate of 1 Hz. Command pulses were generated by a 16-bit Digidata 1320A D/A converter (Molecular Devices) controlled by pCLAMP8.0.2 software (Molecular Devices). Data acquisition and analysis were performed using the Clampex and Clampfit module of pCLAMP software, respectively. Recordings were filtered at 10 kHz and acquired at 100 kHz and stored on the hard disk of a computer for subsequent analysis. Electrode junction potentials (5–10 mV) were measured and nulled before suction of the cell. A high resistance seal (5–10 GΩ) was obtained before the disruption of the membrane patch. After forming the whole-cell recording configuration, a capacitive transient induced by a 10 mV step from a holding voltage of 0 mV was recorded and used for the calculation of cell capacitance. Series resistance ($R_s$) was in the range of 4–6 MΩ and was compensated by 60% to 80%. The calculated average membrane capacitance of LV myocytes from diabetic rats (178.7 ± 7.8 pF, $n$ = 30 cells/9 rats; $P < 0.01$) was smaller than that of

controls (218.9 ± 10.7 pF, $n$ = 26/6). Treatment with AG tended to reduce cell capacitance further in diabetic animals (168.2 ± 7.2 pF, $n$ = 25/7; $P < 0.01$ vs Con+Veh and $P > 0.05$ vs DM+Veh group) with no change in controls (200.0 ± 9.1 pF, $n$ = 25/6, $P > 0.05$ vs Con+Veh).

To study $K^+$ currents, pipettes were filled with normal $K^+$ containing internal solution (mM): KCl 120, NaCl 10, MgATP 5, EGTA 5, and HEPES 10, and pH 7.2 titrated with KOH. During measurement of $K^+$ currents, $Na^+$ and $Ca^{2+}$ inward currents were blocked by addition of 30 μM tetrodotoxin and 1 mM $CoCl_2$ to the bathing solution, respectively. For measurement of $Ca^{2+}$ inward current, the $K^+$ currents were blocked by adding CsCl (2 mM) to the bathing medium and internal dialysis of the cells with $Cs^+$ and tetraethylammonium (TEA)-containing pipette solution (in mM): CsCl 130.0, EGTA 5.0, TEA chloride 15.0, dextrose 5.0 and HEPES 10.0, adjusted to pH 7.2 with CsOH.

***Pulse protocol and analysis***

$K^+$ currents were elicited with depolarizing or hyperpolarizing steps from a holding potential of –80 mV to test potentials ranging between –140 and +60 mV (20-mV steps, 400-ms duration) with a stimulation frequency of 0.2 Hz. Voltages from –30 mV to positive activated a peak outward $K^+$ current and subsequently inactivated to a sustained level ($I_{SS}$) at the end of the pulse. A rapidly activating and inactivating $I_{to}$ was identified as the difference between the peak and the steady-state current ($I_{SS}$). Voltages negative to –60 mV activated an inward current that represented the inward rectifier $K^+$ current ($I_{K1}$). To obtain the steady-state inactivation curves of $I_{to}$, a double-pulse protocol was used consisting of a first conditioning 400-ms pulse from –80 mV to various potentials ranging from –80 to +10 mV, followed by a 200-ms test pulse to +60 mV. The relative peak amplitudes of $I_{to}$ ($I_{to}/I_{to,\,max}$) were plotted against prepulse potentials, and fitted to Boltzmann function and the voltage for half-inactivation ($V_h$) and slope factor ($k$) were calculated. To obtain the recovery curves of $I_{to}$ from inactivation, a paired-pulse protocol was used consisting of two identical 200-ms depolarizing pulses to +60 mV from a holding potential of –80 mV. The prepulse–test pulse interval was varied between 10 and 550 ms. Each paired-pulse sequence was separated by a 10-s interval to allow for complete recovery of $I_{to}$ from inactivation. The normalized recovery fraction of $I_{to}$ ($I_{test\ pulse}/I_{prepulse}$) was plotted against the recovery times and fitted to a monoexponential function.

L-type $Ca^{2+}$ currents ($I_{Ca,L}$) were evoked by applying the depolarizing steps to test potentials ranging between –40 and +60 mV (10-mV steps, 250-ms duration) from a holding potential of –80 mV, after a 150-ms prepulse to –40 mV to inactivate $I_{Na}$ and T-type $Ca^{2+}$ current. Steady-state inactivation of $I_{Ca,L}$ was examined with a double-pulse protocol: 1-s conditioning pulses were applied

in 10-mV steps between –60 to +20 mV from a holding potential of –80 mV, and then the test pulse of 200-ms duration was applied to 0 mV (interpulse duration was 30 ms). The relative peak amplitudes of $I_{Ca,L}$ were plotted against prepulse potentials and fitted to Boltzmann distribution. To obtain the recovery curves of $I_{Ca,L}$ from inactivation, a paired-pulse protocol was used consisting of two identical 250-ms depolarizing pulses to 0 mV from a holding potential of –40 mV. The prepulse–test pulse interval was varied between 40 and 4050 ms. Each paired-pulse sequence was separated by a 10-s interval to allow for complete recovery of $I_{Ca,L}$ from inactivation. The normalized recovery fraction of $I_{Ca,L}$ ($I_{test\ pulse}/I_{prepulse}$) was plotted against the recovery times and fitted to a bi-exponential function.

Steady-state inactivation data of voltage-activated ion channels were fitted with a Boltzmann function of the form:

$$I/I_{max} = 1/\{1+\exp[(V_m-V_h)/k]\}$$

where $I$ gives the current amplitude and $I_{max}$ its maximum, $V_m$ the potential of prepulse, $V_h$ the half-maximal inactivation potential, and $k$ the slope factor. Conductance of voltage-activated ion channel ($G$) was calculated according to the equation as follows:

$$G = I/(V_m-V_{rev})$$

where $I$ is the peak ionic current, $V_{rev}$ is the reversal potential of this current, and $V_m$ is the test potential. The normalized $G$ ($G/G_{max}$) was plotted as a function of $V_m$ (activation curve) and analyzed by using the Boltzmann equation as follows:

$$G/G_{max} = 1/\{1+\exp[(V_h-V_m)/k]\}$$

where $G_{max}$ is the maximal ionic conductance, and $V_h$ and $k$ represent the half-maximal activation potential and a slope factor, respectively.

## Supplemental references

Nguyen T, El Salibi E, and Rouleau JL (1998) Postinfarction survival and inducibility of ventricular arrhythmias in the spontaneously hypertensive rat: effects of ramipril and hydralazine. *Circulation* **98**: 2074–2080.

Chang GJ, Yeh YH, Lin TP, Chang CJ, and Chen WJ (2014) Electromechanical and atrial and ventricular antiarrhythmic actions of CIJ-3-2F, a novel benzyl-furoquinoline vasodilator in rat heart. *Br J Pharmacol* **171**: 3918–3937.

## Supplemental figures and table

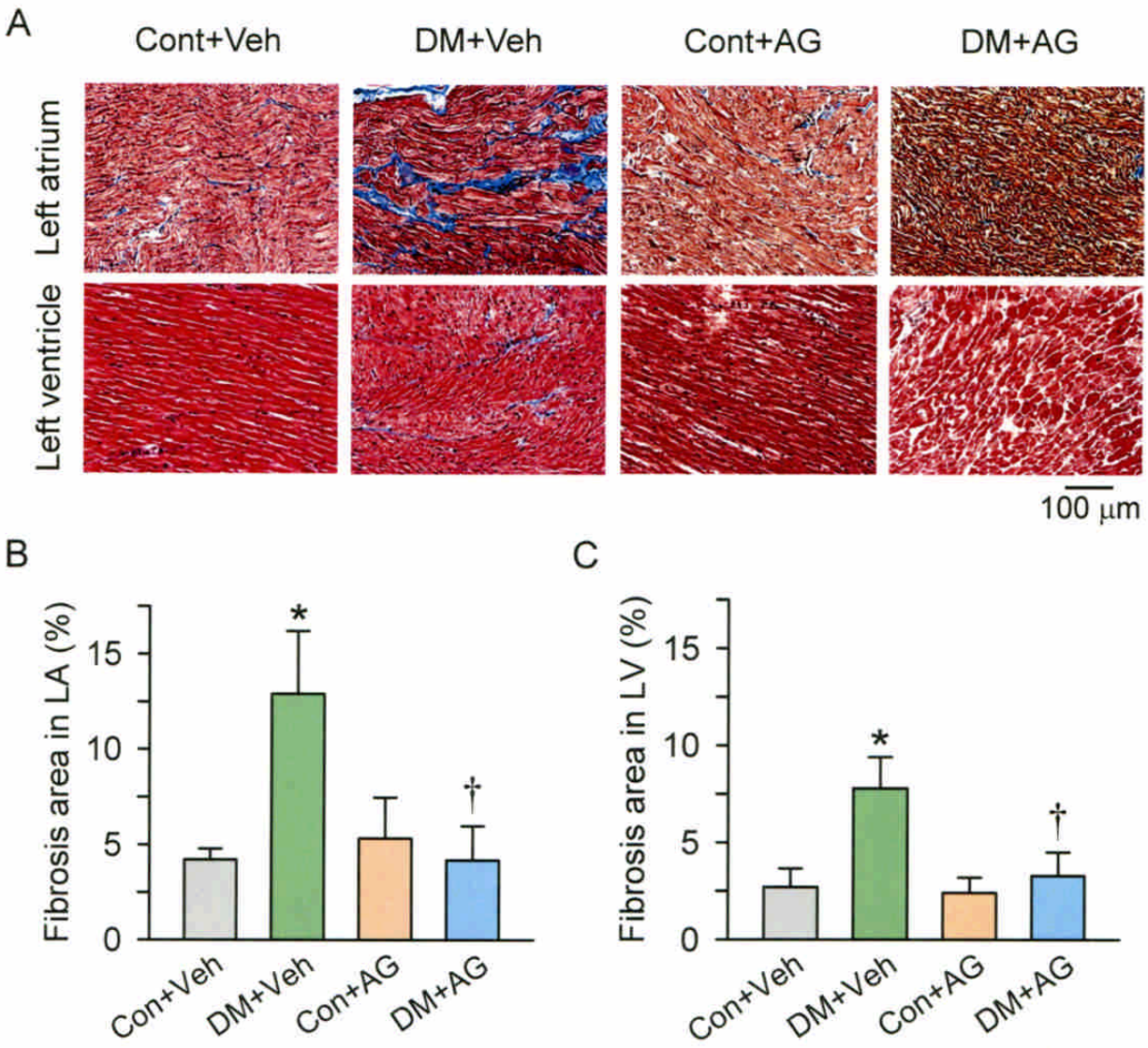


**Supplemental Fig. S1.** Histology of the left atrial (LA) and ventricular (LV) free wall from control (Con) and diabetic (DM) rats with vehicle (Veh) or AG treatment. (A) Representative histological sections of the LA (upper panel) and LV (lower panel) free wall from each group stained with Masson's trichrome (magnification 200×). (B and C) Percent interstitial fibrosis area at LA and LV sections, respectively, calculated as percentage of image accounted for by blue pixels, in each group ($n$ = 7 hearts per group). Values are means ± SEM. *$P$<0.05 vs. Con+Veh group. †$P$<0.05 vs. DM+Veh group.

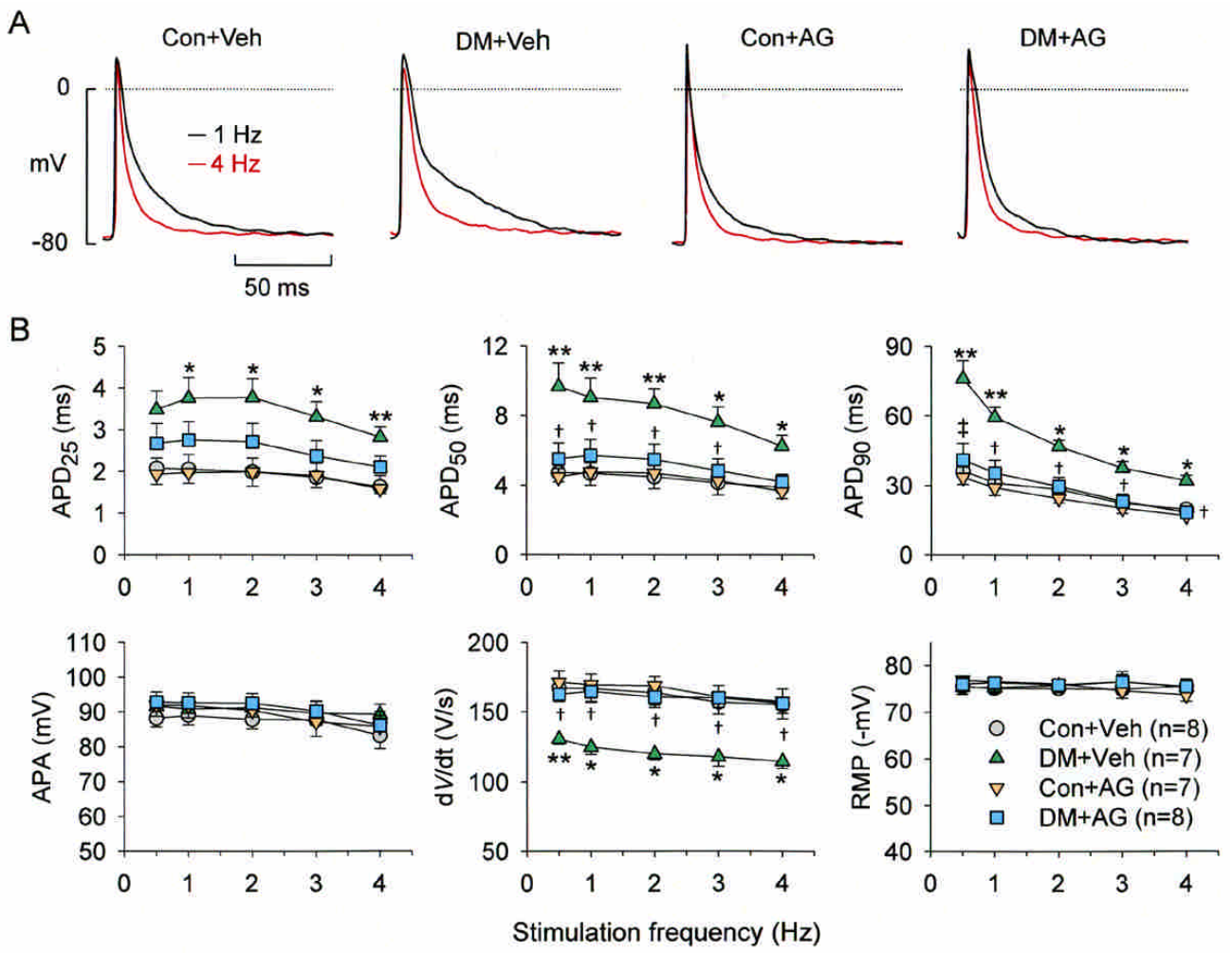


**Supplemental Fig. S2.** Rate-dependence of action potential (AP) recorded in left atrial strips isolated from hearts of various groups. (A) Representative AP traces recorded at 1 and 4 Hz from various groups. (B) Effects of increased stimulus frequency (0.5–4 Hz) on AP duration (APD) at the 25%, 50% and 90% repolarization levels, AP amplitude, maximal depolarization velocity ($V_{max}$), or resting membrane potential (RMP) in various groups. Values are means ± SEM. **P*<0.05 and ***P*<0.01 vs. Con+Veh group. †*P*<0.05 and ‡ *P*<0.01 vs. DM+Veh group.

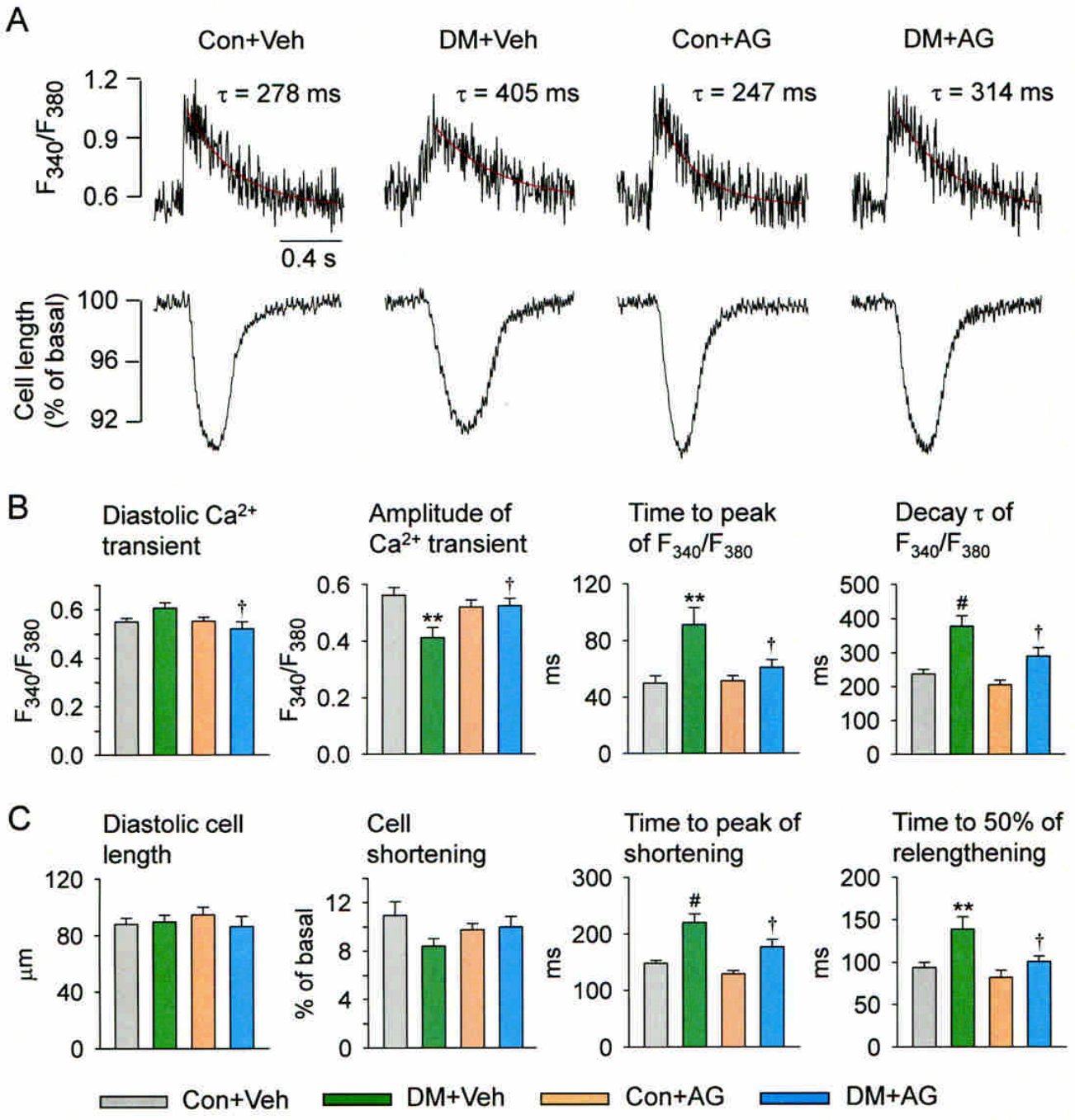


**Supplemental Fig. S3.** Intracellular $Ca^{2+}$ transients and contractile properties of atrial myocytes isolated from hearts of various groups. (A) Representative $Ca^{2+}$ transients (fura-2 fluorescence ratio $F_{340}/F_{380}$, upper panel) with fitted curves and cell-shortening (lower panel) traces of atrial myocytes isolated from various groups stimulated at 1 Hz. (B and C) Intracellular $Ca^{2+}$ transient (B) and contraction (C) properties of myocytes isolated from Con+Veh ($n$ = 16 myocytes/4 rats), DM+Veh ($n$ = 17/6), Con+AG ($n$ = 15/4) and DM+AG ($n$ = 14/5) groups. Values are means ± SEM. **$P$ < 0.01 and #$P$ < 0.001 vs. Con+Veh group. †$P$ < 0.05 vs. DM+Veh group.

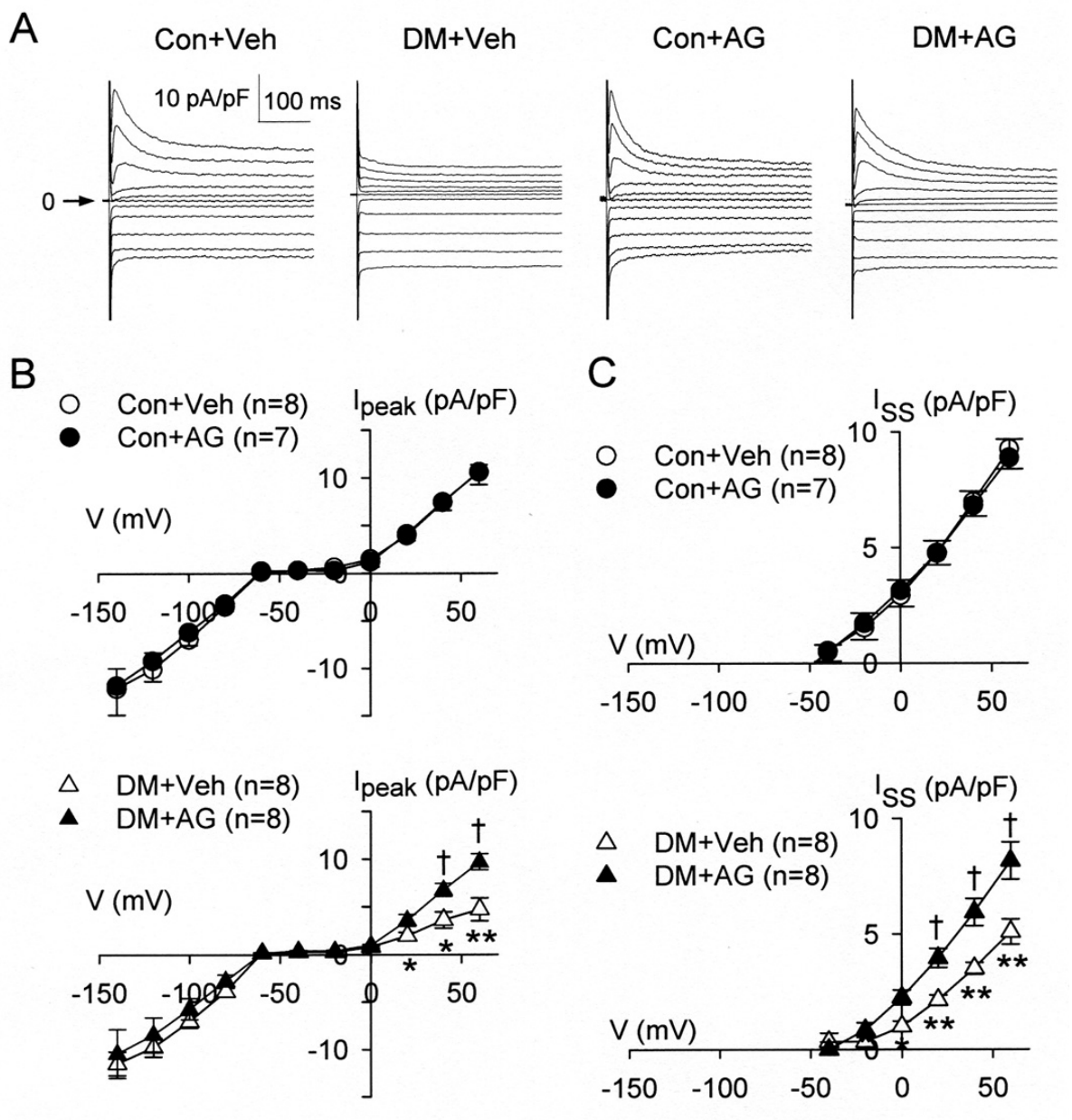


**Supplemental Fig. S4.** Whole-cell $K^+$ currents recorded in atrial myocytes from control and diabetic rats treated with vehicle or AG. (A) Representative normalized whole-cell $K^+$ current traces from Con+Veh (82 pF), Con+AG (112 pF), DM+Veh (108 pF), and DM+AG (83 pF) group. (B) Average current density–voltage (*I–V*) relationships of $I_{to}$ and $I_{K1}$ peak currents. $I_{to}$ was measured as the difference between the peak current and the steady-state current at the end of the pulse. (C) Average *I–V* relationships of $I_{SS}$ current. $I_{SS}$ was measured as the steady-state current at the end of the pulse. Each point is the means ± SEM from individual group cells. **P*< 0.05 and ***P* < 0.01 vs. Con+Veh group. †*P* < 0.05 vs. DM+Veh group.

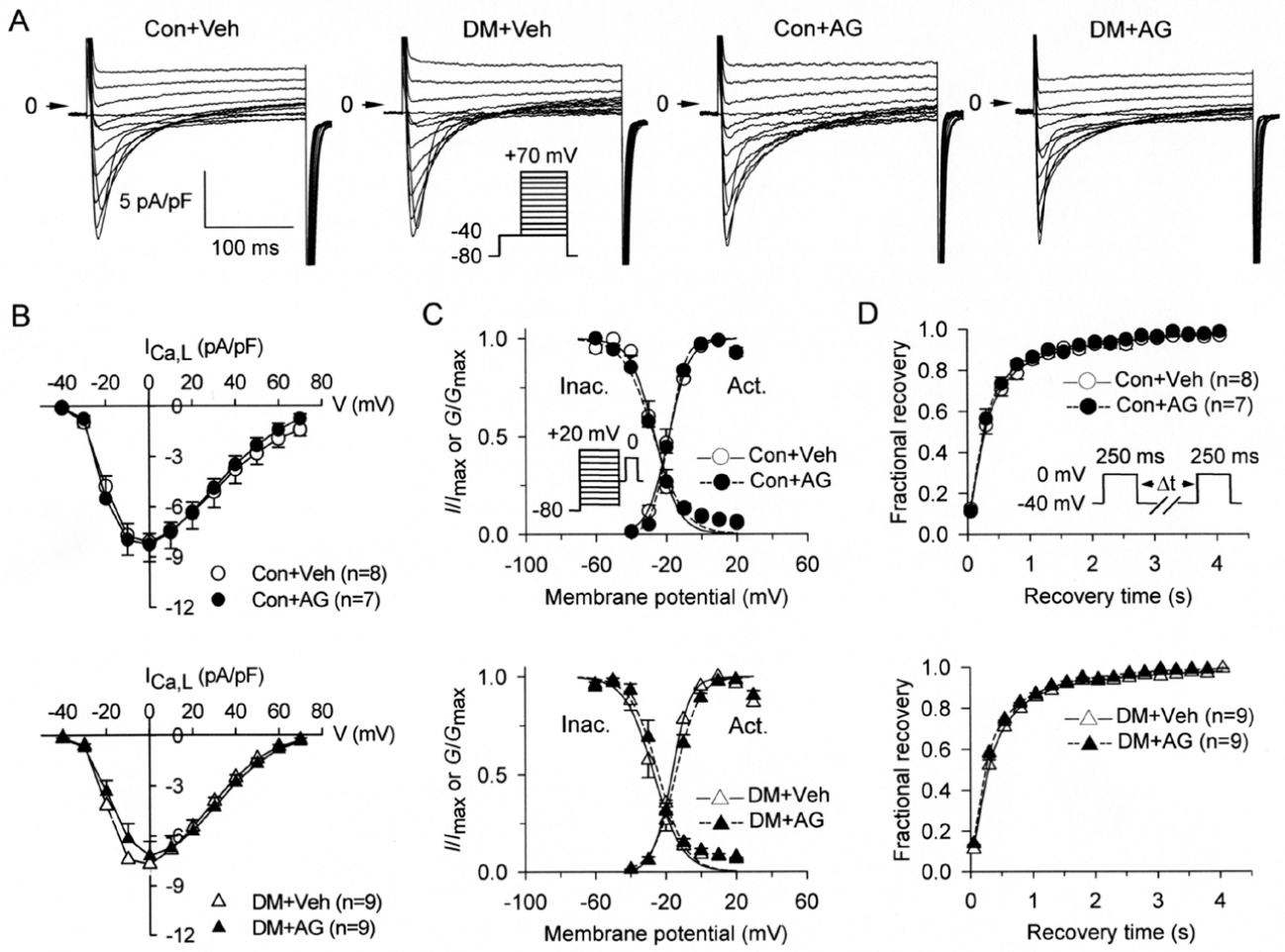


**Supplemental Fig. S5.** L-type $Ca^{2+}$ currents ($I_{Ca,L}$) recorded in LV myocytes from control and diabetic rats treated with vehicle or AG. (A) Representative normalized $I_{Ca,L}$ tracings from Con+Veh (246 pF), Con+AG (227 pF), DM+Veh (162 pF), and DM+AG (157 pF) group. Arrow indicates zero current density level. (B) Averaged *I–V* relationships of $I_{Ca,L}$. The amplitude of $I_{Ca,L}$ was measured as the difference between the peak current and the current at the end of the pulse. Each point is the means ± SEM from individual group cells. (C) Steady-state activation (Act.) and inactivation (Inac.) curves of $I_{Ca,L}$ from various groups. The activation curves were derived using *I–V* curves shown in panel B. Steady-state inactivation was examined with a double-pulse protocol (inset). The relative peak amplitudes of $I_{Ca,L}$ were plotted against prepulse potentials. Solid and dashed line curves shown are fits of mean data from myocytes treated with vehicle or AG, respectively, to Boltzmann distribution. Each point is the means ± SEM from individual group cells. The number of myocytes used for activation and inactivation studies are 8 and 8, 7 and 7, 8 and 9, and 9 and 9, in Cont+Veh, Con+AG, DM+Veh, and DM+AG group, respectively. (D) Recovery of $I_{Ca,L}$ from inactivation was determined with the paired-pulse protocol as shown in the inset. The normalized recovery fraction of $I_{Ca,L}$ ($I_{test\ pulse}/I_{prepulse}$) was plotted against the recovery times. Data are means ± SEM. Solid and dashed lines represent fitting of data points from myocytes treated with vehicle or AG, respectively, with a bi-exponential function.

**Supplemental Table S1**

Kinetic parameters of steady-state activation and inactivation and recovery of $I_{to}$ or $I_{Ca,L}$ from various groups

| | Con+Veh | DM+Veh | Con+AG | DM+AG |
|---|---|---|---|---|
| ***$I_{to}$*** | | | | |
| Activation | | | | |
| *n* | 8 | 10 | 9 | 9 |
| $G_{max}$ (pS/pF) | 101.6 ± 13.9 | 36.1 ± 7.9** | 109.5 ± 12.2 | 81.4 ± 13.4† |
| $V_h$ (mV) | –2.4 ± 2.4 | 2.8 ± 2.3 | –0.7 ± 4.0 | 1.1 ± 1.6 |
| *k* (mV) | 15.0 ± 0.8 | 16.7 ± 1.5 | 17.2 ± 1.6 | 15.8 ± 1.8 |
| Inactivation | | | | |
| *n* | 7 | 9 | 7 | 9 |
| $V_h$ (mV) | –39.5 ± 3.3 | –37.2 ± 3.9 | –40.0 ± 3.5 | –37.7 ± 2.3 |
| *k* (mV) | –5.3 ± 0.3 | –5.9 ± 0.4 | –5.4 ± 0.6 | –6.0 ± 0.4 |
| Recovery | | | | |
| *n* | 8 | 9 | 7 | 8 |
| τ (ms) | 42.5 ± 3.1 | 57.5 ± 7.4 | 45.6 ± 8.2 | 52.3 ± 10.0 |
| ***$I_{Ca,L}$*** | | | | |
| Decay | | | | |
| *n* | 8 | 9 | 7 | 9 |
| $\tau_1$ (ms) | 13.0 ± 1.5 | 18.7 ± 2.0 | 13.0 ± 2.7 | 13.4 ± 1.3 |
| $\tau_2$ (ms) | 74.0 ± 7.4 | 74.1 ± 7.1 | 70.0 ± 8.0 | 73.7 ± 10.1 |
| Activation | | | | |
| *n* | 8 | 8 | 7 | 9 |
| $G_{max}$ (pS/pF) | 111.8 ± 12.2 | 113.7 ± 10.8 | 124.3 ± 12.6 | 111.6 ± 10.8 |
| $V_h$ (mV) | –18.3 ± 1.6 | –16.8 ± 0.8 | –17.9 ± 2.1 | –14.4 ± 1.2 |
| *k* (mV) | 5.8 ± 0.6 | 5.1 ± 0.3 | 4.6 ± 0.6 | 6.2 ± 0.4 |
| Inactivation | | | | |
| *n* | 8 | 9 | 7 | 9 |
| $V_h$ (mV) | –25.5 ± 1.3 | –26.2 ± 2.4 | –27.5 ± 2.7 | –24.7 ± 2.1 |
| *k* (mV) | –6.3 ± 0.2 | –6.4 ± 0.3 | –6.5 ± 0.3 | –6.1 ± 0.2 |
| Recovery | | | | |
| *n* | 8 | 9 | 7 | 9 |
| $A_f$ | 0.74 ± 0.04 | 0.80 ± 0.03 | 0.78 ± 0.03 | 0.76 ± 0.08 |
| $\tau_f$ (s) | 0.30 ± 0.04 | 0.34 ± 0.03 | 0.29 ± 0.03 | 0.26 ± 0.04 |
| $\tau_s$ (s) | 2.05 ± 0.31 | 2.07 ± 0.25 | 1.83 ± 0.25 | 2.08 ± 0.57 |

Data are expressed as mean ± SEM. *n* is number of experiments. $G_{max}$, maximal conductance; $\tau_1$ and $\tau_2$ indicate fast and slow time constant for channel inactivation measured at 0 mV, respectively; $V_h$ and *k* indicate half-activation or inactivation voltage and slope factor; $A_f$ indicates the fast fraction of channel recovery. $\tau_f$ and $\tau_s$ indicate fast and slow time constant for channel recovery, respectively.

**$P$<0.01 vs. Con+Veh group. †$P$<0.05 vs. DM+Veh group.